

Disruption of Dark Matter Minihaloes in the Milky Way environment: Implications for Axion Miniclusters and Early Matter Domination

Xuejian Shen¹, Huangyu Xiao², Philip F. Hopkins¹, Kathryn M. Zurek³

¹ TAPIR, California Institute of Technology, Pasadena, CA 91125, USA

² Department of Physics, University of Washington, Seattle, WA 98195, USA

³ Walter Burke Institute for Theoretical Physics, California Institute of Technology, Pasadena, CA 91125, USA

27 October 2022

ABSTRACT

Many theories of dark matter beyond the Weakly Interacting Massive Particles (WIMP) paradigm feature an enhanced matter power spectrum on sub-parsec scales, leading to the formation of dense dark matter minihaloes. Future local observations are promising to search for and constrain such substructures. The survival probability of these dense minihaloes in the Milky Way environment is crucial for interpreting local observations. In this work, we investigate two environmental effects: stellar disruption and (smooth) tidal disruption. These two mechanisms are studied using semi-analytic models and idealized N-body simulations. For stellar disruption, we perform a series of N-body simulations of isolated minihalo-star encounters to test and calibrate analytic models of stellar encounters before applying the model to the realistic Milky Way disk environment. For tidal disruption, we perform N-body simulations to confirm the effectiveness of the analytic treatment. Finally, we propose a framework to combine the hierarchical assembly and infall of minihaloes to the Milky Way with the late-time disruption mechanisms. We make predictions for the mass functions of minihaloes in the Milky Way. The survival fraction of dense dark matter minihaloes, *e.g.* for axion miniclusters and minihaloes from Early Matter Domination, is $\sim 60\%$ with the relatively low-mass, compact population surviving. The survival fraction is insensitive to the detailed model parameters. We discuss various implications of the framework and future direct detection prospects.

Key words: dark matter – cosmology: miscellaneous – methods: numerical – Galaxy: kinematics and dynamics – solar neighbourhood

1 INTRODUCTION

The gravitational clustering of dark matter has been well measured on galactic scales and super-galactic scales and is consistent with a nearly scale-invariant spectrum of primordial fluctuations (*e.g.* Aghanim et al. 2020). However, the matter power spectrum on extremely small scales ($k \gtrsim \text{pc}^{-1}$), which corresponds to sub-planetary-mass structures, is still weakly constrained and is sensitive to both the nature of dark matter and the thermal history of the early Universe. There have been proposals to detect small scale structures in the mass range $\sim 10^{-13} - 10^2 M_{\odot}$ in the future with Pulsar Timing Arrays (PTAs; *e.g.*, Siegel et al. 2007; Baghran et al. 2011; Dror et al. 2019; Ramani et al. 2020; Lee et al. 2021a,b) and lensing effects (*e.g.*, Kolb & Tkachev 1996; Metcalf & Madau 2001; Diaz Rivera et al. 2018; Fairbairn et al. 2018; Katz et al. 2018; Van Tilburg et al. 2018; Dai & Miralda-Escudé 2020).

Many well-motivated dark matter theories can leave unique fingerprints on the primordial perturbations at small scales¹ ($k \gtrsim \text{pc}^{-1}$), such as the quantum chromodynamics (QCD) axion/axion-like particles (ALPs) with the Peccei-Quinn (PQ) symmetry (Peccei & Quinn

1977) broken after inflation (*e.g.*, Hogan & Rees 1988; Kolb & Tkachev 1993; Kolb & Tkachev 1994; Zurek et al. 2007), Early Matter Domination (EMD; *e.g.*, Erickcek & Sigurdson 2011; Fan et al. 2014) and vector dark matter produced during inflation (*e.g.*, Nelson & Scholtz 2011; Graham et al. 2016). Therefore, small dark matter substructures provide unique insights into the microphysics of dark matter. The model space of interest here differs from that in more common WIMP-like collisionless cold dark matter (CDM) models. In those models, adiabatic fluctuations produced at the end of inflation can also seed small CDM subhaloes down to the kinetic decoupling and free-streaming limit ($k \sim O(\text{pc}^{-1})$), roughly corresponding to the Earth mass ($\sim 10^{-6} M_{\odot}$; *e.g.*, Hofmann et al. 2001; Berezhinsky et al. 2003; Green et al. 2005; Loeb & Zaldarriaga 2005). The evolution of these subhaloes in the Milky Way environment has been studied in the past (*e.g.*, Angus & Zhao 2007; Goerdt et al. 2007; Green & Goodwin 2007; Zhao et al. 2007; Schneider et al. 2010; Berezhinsky et al. 2014; Delos 2019; Facchinetti et al. 2022). However, WIMP-like CDM formed its first non-linear structures at relatively late times with correspondingly low density (*e.g.* $z \sim 60 \ll z_{\text{eq}}$ as shown in Green et al. 2005), and the minihaloes are thus subject to significant disruption due to tidal stripping and disk shocking after falling onto their host haloes (*e.g.*, Ostriker et al. 1972; Gnedin et al. 1999; Goerdt et al. 2007; Zhao et al. 2007; Schneider et al. 2010). The typical minihaloes of WIMP-like CDM are out of

¹ We note that the “small scale” here is fundamentally different from the small-scale problem of CDM (at kpc scale) discussed in astrophysical studies (see review by Bullock & Boylan-Kolchin 2017).

reach for PTAs and other observations we discuss here (*e.g.*, Lee et al. 2021a).

On the other hand, dark matter minihaloes in the theories we consider here formed in the early Universe. Therefore, they are much denser and less likely to be disrupted by tidal forces than WIMP-like CDM subhaloes. For instance, a (pseudo)scalar field (*e.g.* the QCD axion) with the PQ symmetry broken after inflation (*e.g.*, Hogan & Rees 1988; Zurek et al. 2007, hereafter called the “post-inflationary axion”) can induce order-unity isocurvature fluctuations on the horizon scale during the symmetry breaking. Regions with order-unity overdensities tend to collapse gravitationally very early, even before matter-radiation equality ($z_{\text{eq}} \sim 3000$), into small axion miniclusters (AMCs). The miniclusters underwent subsequent hierarchical clustering until the large-scale adiabatic perturbations intervened. As another example, EMD models can introduce a non-standard thermal history that is not constrained by any current data, but adiabatic fluctuations within the horizon can grow during this early period of matter domination. The characteristic mass of dark matter minihaloes formed in early matter domination models is determined by the reheating temperature of this period. In vector dark matter models, the longitudinal modes of the vector DM produced at the end of inflation give rise to a peak in the matter power spectrum on small scales, with the scale directly determined by the dark matter particle mass (Graham et al. 2016; Lee et al. 2021a). Those models have interesting dynamics in the early Universe, which are difficult to probe directly. However, the remnants of those early Universe dynamics, dark matter minihaloes, may be detectable in local observations (*e.g.*, Dror et al. 2019; Ramani et al. 2020; Lee et al. 2021a).

While the evolution of (some versions of) these dark matter minihaloes in the non-linear regime has been studied both semi-analytically with the Press-Schechter model (Zurek et al. 2007; Fairbairn et al. 2018; Enander et al. 2017; Blinov et al. 2020; Lee et al. 2021a; Blinov et al. 2021) and numerically with N-body simulations (Zurek et al. 2007; Buschmann et al. 2020; Eggemeier et al. 2020; Xiao et al. 2021), the gravitational interactions between dark matter minihaloes and the large-scale dark matter structures or baryonic structures are not well studied, due to the large dynamic range and non-linear behaviors involved. Dark matter minihaloes formed from non-standard early universe dynamics can be as light as $\sim 10^{-12} M_{\odot}$, while the Milky Way has a halo mass of $\sim 10^{12} M_{\odot}$. Therefore it is challenging to resolve these small structures while simultaneously simulating the dynamics of the largest structures. However, it is critical to study the survival probability of minihaloes in the Milky Way and to determine the prospects of detecting such structures in the local environment.

Recently, Kavanagh et al. (2020) made an analytic estimate of the effects of stellar disruption on AMCs. However, the study neglects some important non-linear effects, such as the realistic minihalo concentration distribution and multiple channels for disruption. In this paper, we improve these estimates with detailed numerical simulations and semi-analytic treatment to combine all the expected dominant disruption terms. To deal with the enormous dynamic range involved, our strategy is to numerically simulate the dynamics of the dark matter minihaloes in individual encounters (varying *e.g.* halo parameters and impact parameters), using these to build detailed semi-analytic models which can be used to treat the large-scale behavior. This allows us to capture the key non-linear physics on small scales while making realistic predictions for the overall behavior of dark matter minihaloes in the Milky Way galaxy (in ways that can be generalized, in principle, to a broad class of minihalo-like models). Broadly speaking, the disruption of dark matter minihaloes in the Milky Way can be divided into two parts: stellar disruption and tidal

disruption. The stellar disruption term is sensitive to close encounters with individual stars, while the tidal term depends on the gradient of the collective gravitational potential on large scales. We study these separately using N-body simulations and then combine them using semi-analytic models.

This paper is organized as follows. In Section 2, we discuss the minihalo mass function, mass-concentration relation, and the analytic models for stellar disruptions due to individual stellar encounters and tidal disruptions. In Section 3, we present our numerical results from a series of idealized N-body simulations for isolated minihaloes encountering a star, and simulations of tidal stripping. In Section 4, we apply the semi-analytic model calibrated using idealized simulations to a realistic Milky Way environment and combine both stellar disruption and tidal disruption. In Section 5, we study the survival fraction of dark matter minihaloes by applying the framework to different physical models.

We assume a Λ CDM cosmology with parameters given as $h=0.697$, $\Omega_{\text{m}} = 0.2814$, and $\Omega_{\Lambda} = 0.7186$, and adopt scalar spectral index $n_s = 0.9667$. These are consistent with the recent Planck results (Aghanim et al. 2020), and our conclusions are relatively insensitive to variations in these parameters (compared to the much larger uncertainties in *e.g.* minihalo properties from different physical models).

2 ANALYTIC MODEL

2.1 Initial mass functions and concentrations of small-scale structures

The two models discussed in the introduction that lead to the formation of dense minihaloes in the early Universe are: i. (pseudo)scalars (*e.g.* the QCD axion) with symmetry broken after inflation (Hogan & Rees 1988; Zurek et al. 2007), and ii. the EMD model (Erickcek & Sigurdson 2011). These two models are physically well-motivated and are also representatives of models enhancing the matter power spectrum at small scales. Although the cosmological perturbations in those models have different origins, they share common features. They are generated at extremely small scales before matter-radiation equality, forming dark matter substructures as light as $10^{-12} M_{\odot}$ ubiquitously, decoupled from the usual adiabatic fluctuations. The model parameters are the axion mass m_a for the AMC model and the reheating temperature T_{rh} for the EMD model. We vary the axion mass from $1.25 \mu\text{eV}$ to $500 \mu\text{eV}$, which is roughly the mass window that can produce the correct dark matter relic abundance, given uncertainties introduced by the axion emission from strings as shown in Buschmann et al. (2022); Gorghetto et al. (2021). On the contrary, the reheating temperature is loosely constrained although T_{rh} cannot be below a few MeV, otherwise Big Bang Nucleosynthesis will be spoiled, see *e.g.* Kawasaki et al. 1999. We study the value from 15 MeV to 120 MeV. We choose the fiducial values $m_a = 25 \mu\text{eV}$ and $T_{\text{rh}} = 30 \text{MeV}$, such that the minihalo mass function in both models peaks at $\sim 10^{-8} - 10^{-7} M_{\odot}$.

The formation of dense substructures from these small-scale perturbations occurs at early times (see Lee et al. 2021a for an analytic study and Xiao et al. 2021 for simulations of axion miniclusters). The formation and hierarchical mergers of minihaloes are described by the redshift-dependent mass function $dn_0/dM(z)$, calibrated by simulations in Xiao et al. (2021). Meanwhile, the minihaloes can fall onto CDM substructures formed from adiabatic perturbations. The redshift of infall, z_i , which occurs after the minihalo formation, defines the time when they stop merging or accretion, owing to the

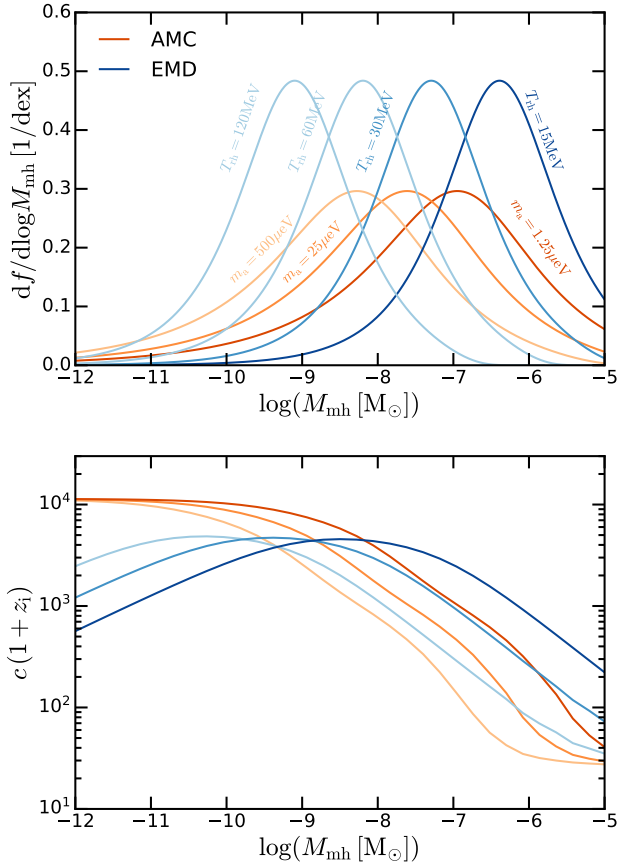


Figure 1. *Top:* Initial (pre-disruption) mass function of minihaloes in different physics models (f is the mass fraction with respect to the total dark matter mass in the Universe). Here we show the mass functions for the AMC models with axion mass $m_a = 1.25, 25, 500 \mu\text{eV}$ and the EMD models with reheating temperature $T_{\text{rh}} = 15, 30, 60, 120 \text{MeV}$. The model parameter variations manifest as constant horizontal shifts of the mass function (see Appendix A for details). The EMD models have sharper peaks than the AMC models. *Bottom:* Mass-concentration relation of minihaloes in different models shown in the top panel. The mass-concentration in the EMD model is peaked due to its peaked matter power spectrum. In general, the halo concentration hits a floor at the massive end as the adiabatic CDM power spectrum takes over. At the low-mass end, since one would not expect minihaloes to form before matter-radiation equality, a cap to the concentration appears at around $c(1+z_i) = 10^4$.

high virial velocities in the normal CDM haloes, and their properties (mass, concentration) remain unchanged afterward.

Therefore, the final mass function, including minihaloes falling onto the CDM structures, can be expressed as

$$\frac{dn_f}{dM}(z) = \int_{z_{\text{eq}}}^z dz_i \frac{df_{\text{col}}^{\text{CDM}}(z_i)}{dz_i} \frac{dn_0}{dM}(z_i) \quad (1)$$

where $f_{\text{col}}^{\text{CDM}}(z)$ is the collapse fraction of normal CDM haloes formed from adiabatic fluctuations. The probability of infall at $z = z_i$ is $\propto \frac{df_{\text{col}}^{\text{CDM}}(z_i)}{dz_i}$, where we have assumed there is no dynamic decoupling between collapsed minihaloes and the overall dark matter content.

We can use the Press–Schechter model (Press & Schechter 1974)

to compute the collapse fraction

$$f_{\text{col}}^{\text{CDM}}(z) = \text{erfc} \left(\frac{\delta_c}{\sqrt{2}\sigma_{\text{CDM}}(M_{\text{min}})D(z)} \right), \quad (2)$$

where $D(z)$ is the growth function, $\sigma_{\text{CDM}}^2(M)$ is the variance of the adiabatic fluctuations calculated using the Code for Anisotropies in the Microwave Background² (CAMB; Lewis et al. 2000; Howlett et al. 2012; Lewis Lewis), and M_{min} is the smallest CDM structure we consider formed from adiabatic fluctuations. There might be even smaller CDM haloes that can form, which will increase the collapse fraction $f_{\text{col}}^{\text{CDM}}(z)$, especially at high redshifts. However, below a certain mass, the normal CDM haloes may have comparable masses to the enhanced substructures, and our assumptions will no longer hold. A detailed study of this infall process will ultimately be required for more detailed predictions and we leave it for future study (treating the mass function as somewhat uncertain below). We take M_{min} to be $10^{-2} M_{\odot}$, corresponding to a scale where the CDM power spectrum dominates while the enhanced small-scale perturbations become subdominant. The result is insensitive to M_{min} as $\sigma(M)$ depends logarithmically on M at small scales. This allows us to compute the collapse fraction at various redshifts analytically and obtain the final mass function for the enhanced substructures. This will also give us the distribution of the infall redshift z_i , $\mathcal{P}(z_i)$ ³, which determines the time when the structural changes of minihaloes halt and thus the average density of minihaloes. Including minihaloes falling onto CDM haloes, we obtain the minihalo mass function at $z = 0$ given the initial mass function from different models, as shown in Figure 1.

Regarding the concentration of minihaloes, we adopt the model in Lee et al. (2021a) to calculate the concentration from the power spectra of different models. For each mass, it evaluates the redshift when the corresponding primordial fluctuation mode collapse (z_c), and assumes $c(M) \propto (1+z_c(M))$ which is similar to the CDM results (e.g., Bullock et al. 2001). The only difference here is that we assume the merger or smooth accretion of minihaloes stops at z_i instead of $z = 0$. Therefore, effectively, we have $c(M) \propto (1+z_c(M))/(1+z_i)$. In Figure 1, we show the initial (pre-disruption) mass functions and the mass-concentration relations of minihaloes in different physics models. At the high mass end, the adiabatic CDM power spectrum will dominate and one should reproduce the mass-concentration relation of normal CDM haloes. There is a cap for concentration at the low-mass end since one will not expect minihalo formation before matter-radiation equality. The axion mass for the AMC models or the reheating temperature of the EMD models only creates constant mass shifts in the mass function and the mass-concentration relation. For reference, the typical concentration of WIMP-like CDM haloes studied in Green & Goodwin (2007) and Delos (2019) are $c \sim 1-20$ at the redshift when minihaloes are initialized (usually $z \sim 60-100$ in these studies). In terms of concentration, they are comparable to the relatively massive minihaloes studied here.

² CAMB documentation

³ Integrated over the entire mass range, $\mathcal{P}(z_i) \propto df_{\text{col}}^{\text{CDM}}(z)/dz$ is purely determined by CDM cosmology. However, if looking at minihaloes at $z = 0$ in a certain mass range, the conditional probability distribution of z_i will be mass dependent. In the hierarchical formation of minihaloes, more massive ones form at later times. Therefore, more massive minihaloes found at $z = 0$ tend to have lower z_i .

2.2 Disruption in late-time evolution

Owing to the ultra-compact structure of the minihaloes, they are largely immune to external perturbations through their evolutionary history after decoupling from the Hubble flow. However, after falling into a massive host system like the Milky Way, non-linear gravitational interactions with the host halo and the dense baryonic structures in the host halo can lead to significant disruption of minihaloes. The two leading disruption mechanisms are tidal disruption from the host halo (and the baryonic disk) and close encounters with stars (referred to as stellar disruption). The relevant spatial and time scales on which these two mechanisms operate are drastically different. In this section, we will review the analytic model developed.

2.2.1 Stellar disruption

First, we consider the consequence of the encounter between a minihalo and a star. The virial radius of minihaloes with a mass of interest ($\sim 10^{-10} M_\odot$) is of the order of 0.01 pc, which is still much larger than the radius of main sequence stars even though we are considering minihaloes. Therefore, for simplicity, stars can be treated as point-like objects during encounters. In addition, after a stellar encounter, the structure of the minihalo cannot immediately react to the energy imparted during the encounter. It takes roughly a dynamical time for the minihaloes to relax to the final state after disruption, which is given by

$$t_{\text{dyn}} = \sqrt{\frac{3\pi}{16G\bar{\rho}_{\text{mh}}}} \approx 0.76 \text{ Gyr} \left(\frac{1+z_i}{3}\right)^{-3/2}, \quad (3)$$

where $\bar{\rho}_{\text{mh}}$ is the average density of the minihalo. The dynamical time t_{dyn} will be comparable to the Hubble time scale for $z_i = 0$ but much shorter than that if the minihaloes fall into CDM structures at a high redshift. The duration of the star-minihalo encounter ($\propto b/v_*$), however, is at least five orders of magnitude shorter than t_{dyn} . Therefore, the impulse approximation holds and the encounter can be treated as an instantaneous interaction (Spitzer 1958). In the distant-tide approximation (when the impact parameter is much larger than minihalo size), the imparted energy from a single star encounter can be expressed as (Spitzer 1958)

$$\Delta E \approx \frac{4}{3} \frac{G^2 m_*^2 M_{\text{mh}} \langle r^2 \rangle}{v_*^2 b^4} = \frac{4\alpha^2}{3} \frac{G^2 m_*^2 M_{\text{mh}} R_{\text{mh}}^2}{v_*^2 b^4}, \quad (4)$$

where ΔE is the increase of internal energy of the minihalo, M_{mh} (R_{mh}) is the virial mass (radius) of the minihalo, $\langle r^2 \rangle$ represents the mean-squared radius of particles with respect to the center of the minihalo. m_* , b , and v_* are the mass, impact parameter, and relative velocity of the stellar object, respectively. The mean-squared radius can be parameterized as $\langle r^2 \rangle = \alpha^2 R_{\text{mh}}^2$, where α is a dimensionless parameter determined by the density profile $\rho(r)$ of the dark matter minihalo

$$\alpha^2 = \frac{\langle r^2 \rangle}{R_{\text{mh}}^2} = \frac{1}{M_{\text{mh}} R_{\text{mh}}^2} \int_0^{R_{\text{mh}}} d^3\mathbf{r} r^2 \rho(r). \quad (5)$$

Assuming that the minihalo has the NFW profile (Navarro et al. 1996, 1997), one obtains

$$\alpha^2(c) = \frac{c(-3 - 3c/2 + c^2/2) + 3(1+c) \ln(1+c)}{c^2(-c + (1+c) \ln(1+c))}, \quad (6)$$

where c is the concentration number of dark matter minihaloes.

However, when the impact parameter becomes comparable to the size of the minihalo, the distant-tide approximation made by Equation 4 breaks down. The strong b^{-4} dependence of ΔE will disappear

once the star passes through the minihalo and the disruption effect is suppressed (e.g., Gerhard & Fall 1983; Moore 1993; Carr & Sakellariadou 1999; Green & Goodwin 2007). For a single encounter, Green & Goodwin (2007) proposed a more general treatment of the imparted energy calibrated using simulations

$$\Delta E = \begin{cases} \frac{4\alpha^2(c)}{3} \frac{G^2 m_*^2 M_{\text{mh}} R_{\text{mh}}^2}{v_*^2} \frac{1}{b^4} & (b > b_s) \\ \frac{4\alpha^2(c)}{3} \frac{G^2 m_*^2 M_{\text{mh}} R_{\text{mh}}^2}{v_*^2} \frac{1}{b_s^4} & (b \leq b_s) \end{cases} \quad (7)$$

where $b_s = f_b (2\alpha/3\beta)^{1/2} R_{\text{mh}}$ is the transition radius, which is close to the physical size of the minihalo up to a factor determined by structure parameters, and f_b is an order-unity correction factor we introduce⁴ to be determined by our simulations, which will be discussed in Section 3. β is another structural parameter defined as

$$\beta^2 = \langle r^{-2} \rangle R_{\text{mh}}^2 = \frac{R_{\text{mh}}^2 \int_{r_c}^{R_{\text{mh}}} d^3\mathbf{r} r^{-2} \rho(r)}{M_{\text{mh}}} \\ \simeq \frac{c^2 \ln(r_s/r_c) + c^2/2 - 1/2}{\ln(1+c) - c/(1+c)}, \quad (8)$$

where the NFW profile is assumed and r_c is the smallest radius that the profile extends to, which we assume to be $0.01 r_s$. In principle, an axion star formed in the center of a minihalo can provide a natural physical scale for r_c . However, the size of an axion star sensitively depends on particle physics parameters as well as the growth rate of axion stars (e.g., Visinelli et al. 2018; Helfer et al. 2017; Chen et al. 2021). We note that the choice of r_c has weak effects since i. it only appears in the logarithm; ii. the uncertainties of r_c and β have been effectively captured by the free parameter f_b ; iii. β in fact only matters for close encounters, which are rare in reality.

Compared to full analytic calculations under the impulse and distant-tide approximations, Equation 7 gives better agreement with simulations in the transitional regime. Roughly speaking, disruption of a minihalo is expected to occur when the increase in internal energy of the minihalo given by Equation 4 exceeds the binding energy of the minihalo

$$E_b = \gamma G M_{\text{mh}}^2 / 2R_{\text{mh}}. \quad (9)$$

Here γ is a dimensionless parameter again determined by the mass profile of the dark matter halo. For the NFW profile, it takes the form (Mo et al. 1998)

$$\gamma(c) = \frac{c}{2} \frac{1 - 1/(1+c)^2 - 2\ln(1+c)/(1+c)}{[c/(1+c) - \ln(1+c)]^2}. \quad (10)$$

Utilizing Equation 7 and 9, we obtain the normalized energy input to the minihalo as

$$\frac{\Delta E}{E_b} = \begin{cases} \frac{4\alpha^2(c)}{3\gamma(c)} \frac{G m_*^2}{v_*^2 b^4} \frac{R_{\text{mh}}^3}{M_{\text{mh}}} = \frac{\alpha^2(c)}{\pi\gamma(c)} \frac{G m_*^2}{v_*^2 b^4} \frac{1}{\bar{\rho}_{\text{mh}}} & (b > b_s) \\ \frac{4\alpha^2(c)}{3\gamma(c)} \frac{G m_*^2}{v_*^2 b_s^4} \frac{R_{\text{mh}}^3}{M_{\text{mh}}} = \frac{3\beta^2(c)}{f_b^4 \gamma(c)} \frac{G m_*^2}{v_*^2} \frac{1}{M_{\text{mh}} R_{\text{mh}}} & (b \leq b_s) \end{cases} \quad (11)$$

⁴ The original formula proposed in Green & Goodwin (2007), who were studying low concentration haloes, does not have the correction term (equivalently $f_b = 1$). However, minihaloes with higher concentrations are studied in this work and we find the correction term is necessary empirically to fit the simulation results.

where $\bar{\rho}_{\text{mh}} = M_{\text{mh}}/(4\pi R_{\text{mh}}^3/3)$ is the average density of the minihalo. Assuming the minihaloes are in virial equilibrium with respect to the background density at redshift z_i (the infall redshift), we obtain $\bar{\rho}_{\text{mh}} = \Delta_c \rho_{\text{crit}}(z_i)$, where $\rho_{\text{crit}}(z_i)$ is the critical density of the Universe at z_i and $\Delta_c = 200$ is the critical overdensity of collapsed objects (we can neglect corrections from *e.g.* Ω_Λ to δ_c at the z_i of interest, so that $\rho_{\text{crit}}(z_i) \propto (1+z_i)^3$). Since $\bar{\rho}_{\text{mh}}$ is independent of minihalo mass, the energy input in the large- b case in Equation 11 will be independent of minihalo mass while having a strong dependence on the impact parameter. The only free parameter that is left to be determined by simulations in Equation 11 is the correction factor f_b .

From Equation 11 (assuming the $b > b_s$ case), we can compute a characteristic impact parameter when $\Delta E/E_b = 1$

$$b_{\text{min}} = \sqrt{\frac{m_*}{v_*}} \left(\frac{\alpha^2(c)G}{\pi\gamma(c)\bar{\rho}_{\text{mh}}} \right)^{1/4} \approx 0.11 \text{ pc} \left(\frac{\alpha^2(c)}{\gamma(c)} \right) \left(\frac{m_*}{1M_\odot} \right)^{1/2} \left(\frac{v_*}{200 \text{ km/s}} \right)^{-1/2} \left(\frac{1+z_i}{3} \right)^{-3/4}, \quad (12)$$

which gives a crude estimate of the condition for the destruction of minihaloes. It is worth noting that the average density of a virialized halo is much larger when formed at higher redshifts, given as $\bar{\rho}_{\text{mh}} \propto (1+z_i)^3$. Minihaloes that collapsed and fell into the host halo earlier in cosmic time should be less vulnerable to stellar disruptions due to higher central densities. Although b_{min} serves as a good indicator for “significant” disruption of the minihalo, the actual mass loss of the minihalo (as a function of $\Delta E/E_b$) after a single encounter will be calibrated by numerical simulations presented in the following section.

2.2.2 Tidal disruption

Another important disruption mechanism for minihaloes is tidal disruption. After the minihaloes fall into the Milky Way halo, they experience tidal forces from the Milky Way dark matter halo and the Galactic disk. In contrast to the stellar disruption, which sensitively depends on close encounters with stars, the tidal forces are determined by gravity at galactic scales, dominated by the collective effects of the smooth gravitational potential rather than the fluctuating component from individual objects. Moreover, rather than an impulsive event, tidal disruption is secular and usually treated differently from stellar disruptions.

In a sufficiently strong and smooth external tidal field, the outskirts of the minihalo will be stripped away where the tidal force exceeds the self-gravity of the minihalo. This tidal radius is given by (*e.g.*, King 1962; Taylor & Babul 2001; Zentner & Bullock 2003a)

$$r_t = R \left[\frac{M_{\text{mh}}(r < r_t)/M_{\text{MW}}(r < R)}{2 - \left. \frac{d \ln M_{\text{MW}}}{d \ln R} \right|_R + \frac{V_t(\mathbf{R})}{V_c(R)}} \right]^{1/3}, \quad (13)$$

where R is the galactocentric distance of the minihalo, $M_{\text{MW}}(r < R)$ is the mass of the Milky Way (including both dark and baryonic matter) enclosed within radius R and $M_{\text{mh}}(r < r_t)$ is the minihalo mass enclosed within r_t . $V_t(\mathbf{R})$ is the instantaneous tangential speed of the minihalo, which equals the circular velocity $V_c(R)$ when the minihalo is on a circular orbit. The minihalo mass outside the tidal radius will be stripped away roughly over a dynamical time scale of the host, and the instantaneous mass-loss rate is often expressed as

(*e.g.*, Taffoni et al. 2003; Zentner & Bullock 2003b; Oguri & Lee 2004; Pullen et al. 2014)

$$\dot{M}_{\text{mh}} = -\frac{M_{\text{mh}}(r > r_t)}{t_{\text{ts}}(R)}, \quad (14)$$

where t_{ts} is the characteristic time scale of tidal stripping, which is proportional to the dynamical time scale of the host halo (not the minihalo)

$$t_{\text{ts}}(R) = A t_{\text{dyn}}^{\text{host}}(R) \approx 90 \text{ Myr} \left(\frac{A}{1} \right) \left(\frac{\bar{\rho}_{\text{host}}(R)}{1.6 \times 10^7 M_\odot \text{ kpc}^{-3}} \right)^{-1/2} \quad (15)$$

where $\bar{\rho}_{\text{host}}(R)$ is the averaged density of the host halo within radius R and A is a constant fudge factor of order unity that is found to be ~ 0.5 -3 in several previous studies (*e.g.*, Zentner & Bullock 2003b; Zentner et al. 2005; Pullen et al. 2014; van den Bosch et al. 2018; Green et al. 2021). If the tidal stripping occurs in the Solar neighborhood, the time scale will be much shorter than the lifetime of minihalo in the Milky Way environment. As a simple estimation, the characteristic formation time (defined as when $d \log M/d \log a$ falls below a threshold as proposed in Wechsler et al. 2002) of a Milky Way-mass halo is about $a_f = 0.3$ (corresponding to $z_f \sim 2.5$ and lookback time $\gtrsim 10$ Gyr). If the minihaloes are dynamically coupled to the smooth dark matter content accreted by the Milky Way halo, the typical lifetime of minihaloes in the Milky Way environment will be of the same order. Therefore, a reasonable assumption is that the minihalo outskirts will be tidally disrupted immediately after infall and before any form of stellar disruptions takes place.

3 IDEALIZED SIMULATIONS FOR STELLAR ENCOUNTERS AND TIDAL STRIPPING

We next use N-body simulations to systematically study the stellar disruption and tidal stripping effects for isolated minihaloes initialized with the NFW profile. The goal is to test the analytic models described in Section 2 and calibrate them with various minihalo parameters.

3.1 Stellar encounters

A suite of N-body simulations is performed for minihaloes initialized with the NFW profile by varying minihalo concentrations, masses, and impact parameters of the encountering stars. The simulations adopt the code GIZMO⁵ (Hopkins 2015), which has been widely used in cosmological N-body or hydrodynamical simulations (*e.g.*, Hopkins et al. 2014, 2018a; Feldmann et al. 2022). These simulations aim to test and calibrate analytic predictions of the minihalo mass fraction disrupted in stellar encounters. The relaxation process of minihaloes and the evolution of density profiles are also studied, which provides important insights in modelling the disruption effects under multiple encounters.

In these simulations, an isolated minihalo (composed of collisionless N-body dark matter particles) is initialized at $z = 0$ ⁶ with a star (represented by a single point-mass particle) having mass $m_* = 1 M_\odot$

⁵ GIZMO documentation

⁶ The simulations are not cosmological, but the redshift value is required for initializing the NFW halo. The response of minihaloes to encounters we test in this section is not sensitive to the density normalization or the redshift we set up the minihalo.

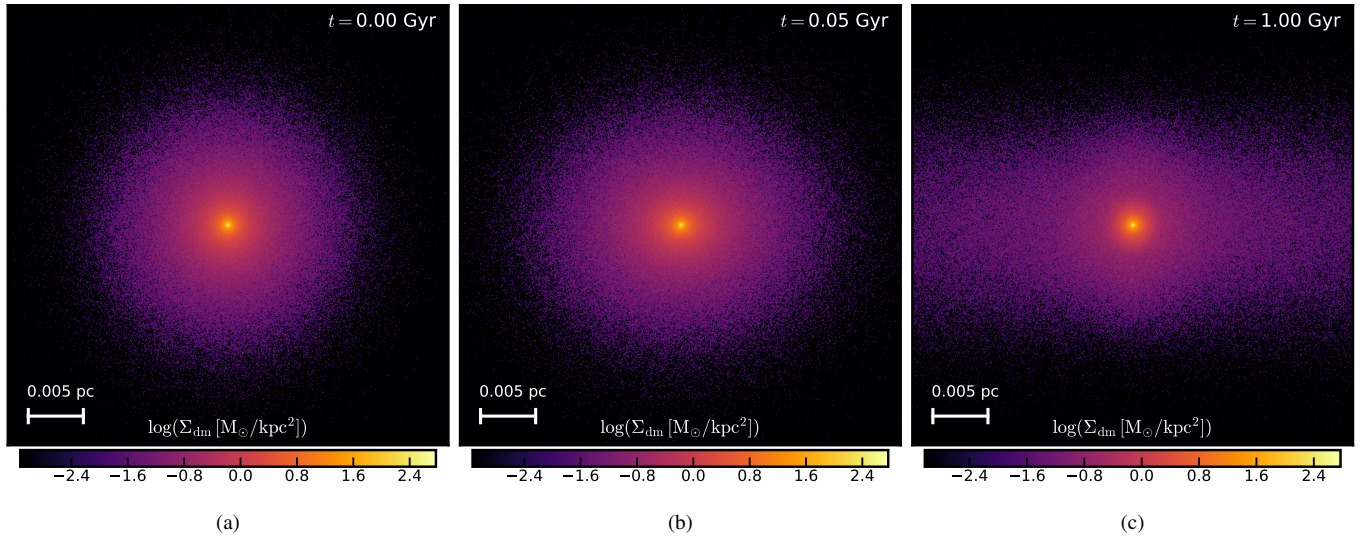


Figure 2. The evolution of a minihalo during stellar disruption is visualized. This is a simulation of an encounter between a minihalo of mass $M_{\text{mh}} = 10^{-10} M_{\odot}$ and a star of mass $m_* = 1 M_{\odot}$, with the impact parameter $b = 10^{-4} \text{kpc}$. The star passed by in the y -direction of the image. We show the dark matter surface density distribution of the minihalo. Figure 2a shows the initial dark matter distribution. Right after the encounter, a large fraction of dark matter has been heated up by the gravitational interaction with the passing star and become unbound. Although this energy is transferred impulsively, it requires roughly the minihalo dynamical time ($t_{\text{dyn}} \gtrsim 1 \text{Gyr}$) for the disruption to be reflected in the minihalo density distribution, as shown in Figure 2b and Figure 2c.

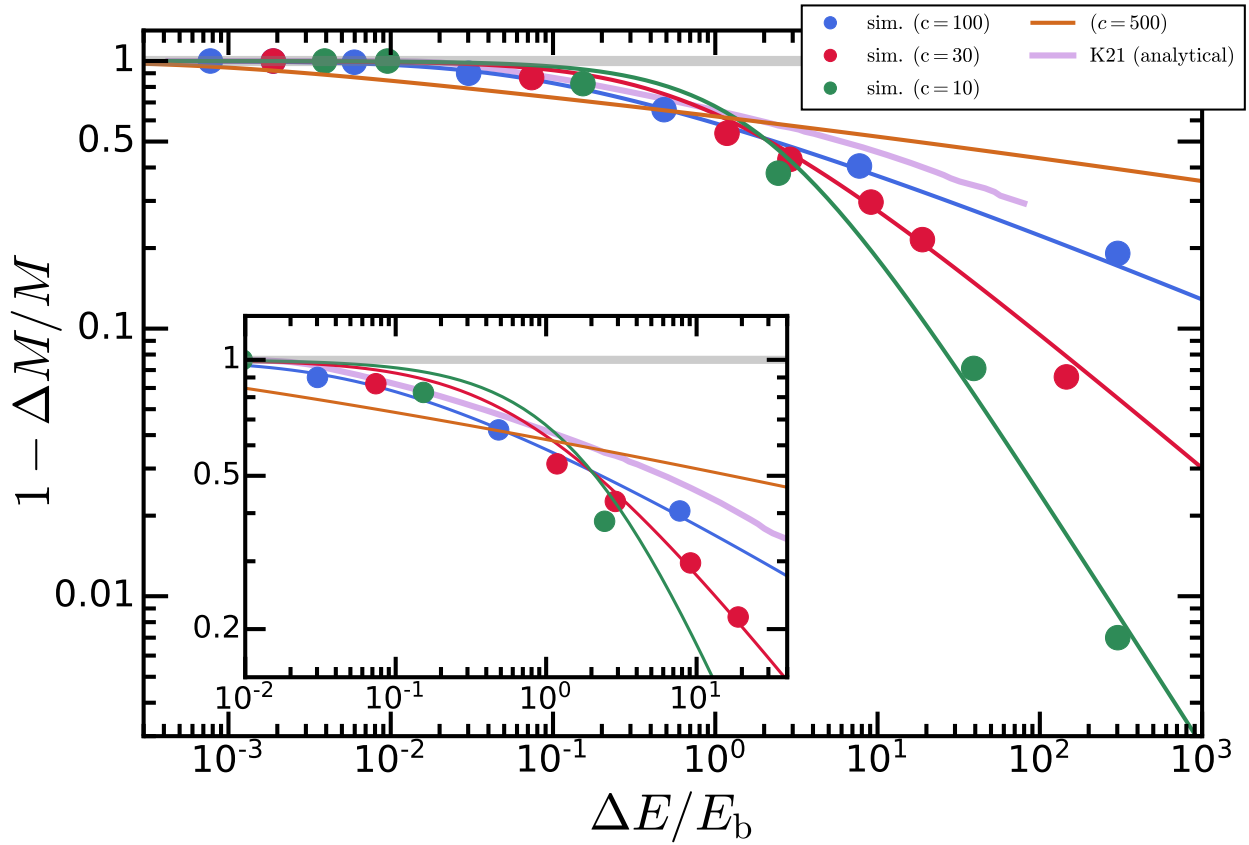


Figure 3. Fractional mass loss as a function of the normalized imparted energy for stellar encounters with minihaloes with $c = 10, 30, 100, 500$. The simulation results are shown in solid points, and the best-fit model is shown in solid lines. For reference, the purple curve is the analytic prediction from [Kavanagh et al. \(2020\)](#) for $c = 100$ minihaloes. The zoom-in subplot shows the transitional regime around $\Delta E/E_b \sim 1$. The response curves calibrated from our simulations are in good agreement with results in [Kavanagh et al. \(2020\)](#). However, the asymptotic behaviour of the response curve at large $\Delta E/E_b$ has a significant concentration dependence, which has not been revealed in previous studies.

at a large distance (10 pc) moving towards the minihalo with a relative velocity of 200 km s^{-1} . Since the code is Lagrangian, it makes no difference whether the star or the minihalo is moving and in which frame we solve the dynamics equations. In Figure 2, the evolution of a minihalo during disruption is visualized. The encounter with a star will impart a certain amount of energy into the minihalo, disrupting the halo outskirts at roughly a minihalo dynamical time. Our default simulations resolve the minihalo with 10^6 dark matter particles initialized in an equilibrium NFW halo following the method in Springel (2005). We generate the initial condition using the package `pyICs`⁷ (Herpich et al. 2017). To systematically study stellar disruption effects, we vary the impact parameter of the star, the minihalo mass, and the minihalo concentration (or equivalently scale radius). The gravitational softening length of the dark matter particles is taken to be 10^{-9} kpc, which is small enough to resolve the dense core of those minihaloes with a mass $10^{-10} M_{\odot}$ and concentration $c = 100$, which have a scale radius $r_s = 9.6 \times 10^{-8}$ kpc. The time-stepping in the simulation requires more careful consideration, since most disruption occurs when the distance between the star and the minihalo is around its minimum. We choose the maximum size of the timestep to be 10^{-8} Gyr even when the star is still at a large distance (10 pc) from the minihalo and study the subsequent disruption as the star moves closer towards the minihalo. It is worth noting that this timestep is about an order of magnitude smaller than the crossing time of the star, $\sim R_{\text{mh}}/v_*$, so that the trajectory of the star around the minihalo can be well resolved. After the close encounter, we can relax the upper limit on the timestep to integrate the relaxation of the minihalo after the stellar disruption to arbitrarily long times (at a fairly low computational cost). A detailed discussion of numerical convergence is given in Appendix B. Experimenting with the maximum timestep and/or the gravitational softening length shows that smaller values produce essentially identical results (with larger computational cost). However, order-of-magnitude larger values of softening length can risk allowing the simulation to “oversmooth” gravity or take excessively large timesteps for some particles, which “overshoot” the very brief duration of the encounter (for detailed numerical tests, see Hopkins et al. 2018b and Grudić & Hopkins 2020).

3.1.1 Disruption under different impact parameters and calibration of the response function

We first run three sets of simulations for encounters with fixed minihalo mass and concentration but different impact parameters. In all these simulations, we set a fixed minihalo mass $M_{\text{mh}} = 10^{-10} M_{\odot}$, star mass $m_* = 1 M_{\odot}$ and initial star-minihalo relative velocity $v_* = 200 \text{ km/s}$. The halo concentration has been fixed to be $c = 10, 30, 100$ for each set of simulations, respectively. The goal is to characterize the relation between the mass loss of the minihalo after a stellar encounter and the normalized energy input. The imparted energy can be related to the impact parameter with Equation 11. After the minihalo becomes fully relaxed after the stellar encounter (at $t = 1 \text{ Gyr} > t_{\text{dyn}}(z = 0)$), dark matter particles, with kinetic energy (in the center-of-momentum frame) larger than the absolute value of their gravitational potential energy, are identified as unbound and disrupted. The remaining mass of the minihalo is measured as the fraction of bound dark matter particles after minihalo relaxation, and we have verified that the remaining minihalo mass has converged at the time of measurement.

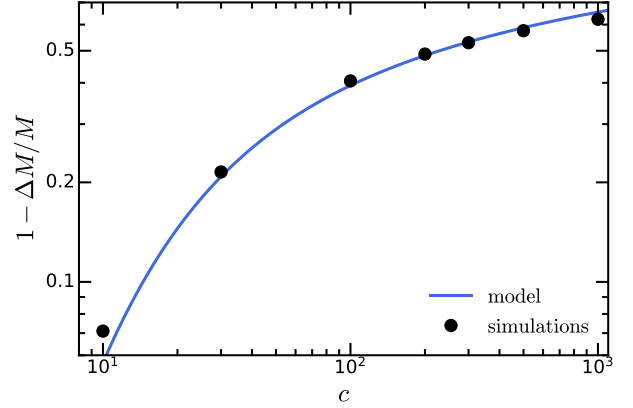


Figure 4. Fractional mass loss as a function of concentration at impact parameter $b = 0.05$ pc. The blue solid curve is the semi-analytic model prediction while the data points are obtained from simulations.

In Figure 3, we show the minihalo mass loss as a function of the normalized imparted energy for different choices of halo concentrations. The imparted energy is calculated using Equation 11 (for the minihalo and impact parameters tested here, the transition radius b_s is always smaller than the impact parameters, so the free parameter f_b does not affect the results). The mass loss is negligible when $\Delta E/E_b \ll 1$, and quickly increases in a power-law fashion with respect to $\Delta E/E_b$. In this regime, minihaloes with low concentrations are more vulnerable to stellar encounters with steeper power-law slopes. In the following, the mass loss as a function of the imparted energy and halo concentration will be referred to as the response curve, $\mathcal{F}(\Delta E/E_b, c)$. We propose the following functional form to fit the response curve

$$\frac{M_{\text{mh}} - \Delta M_{\text{mh}}}{M_{\text{mh}}} \equiv \mathcal{F}(\Delta E/E_b, c) = \frac{2}{1 + \left(1 + \frac{\Delta E/E_b}{p(c)}\right)^{k(c)}}, \quad (16)$$

where $\Delta E/E_b$ should be evaluated using Equation 11 (the free order-unity parameter f_b is yet to be determined, but the calibration here is done in the $b \gg b_s$ regime, so f_b does not have any real impact). After exploring the response curve of each choice of minihalo concentration, we propose the following fitting formula for the parameters $p(c)$ and $k(c)$

$$\begin{aligned} \log p(c) &= a_1 (\log c - \eta) + a_2 (\log c - \eta)^2 + a_3 (\log c - \eta)^3 \\ \log k(c) &= b_0 + b_1 (\log c - 2) \end{aligned} \quad (17)$$

Then we perform the least-square fits jointly to the results of all sets of simulations. The best-fit parameters are $\eta = 0.98$, $a_1 = -0.8$ (fixed), $a_2 = -0.59$, $a_3 = -0.034$, $b_0 = -0.58$, $b_1 = -0.56$. The best-fit model is also shown in Figure 3 and is in good agreement with the simulation results of minihaloes with various concentrations.

This best-fit model of the response curve will be the foundation we use to understand the disruption of minihaloes with different masses or concentrations. We now relax our assumption of a fixed concentration or mass ratio and test this fitted response curve for a wide range of encounters. In Figure 3, we show our best-fit model of the response curve for minihaloes of concentration 10 – 500, and show that the model agrees well with the simulation results.

⁷ `pyICs` documentation

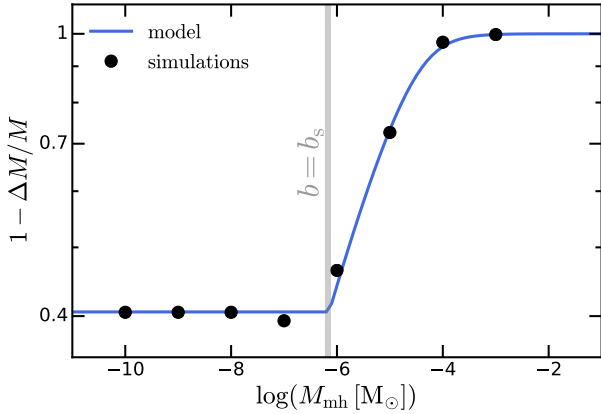


Figure 5. Fractional mass loss as a function of minihalo mass with concentration $c = 100$ and impact parameter $b = 0.05$ pc. The black solid points are simulation results. The blue curve is the semi-analytic prediction using the best-fit response curve.

3.1.2 Disruption under different halo concentrations

Given the calibrated response function, we next run an additional set of simulations with a fixed impact parameter $b = 0.05$ pc but for minihaloes with different concentrations. The goal is to further validate this semi-analytic model (the analytic calculation of imparted energy plus simulation calibrated response function) for minihaloes with various compactness. The minihalo mass is still fixed to $M_{\text{mh}} = 10^{-10} M_{\odot}$ and the properties of the encountering star are the same as in Section 3.1.1.

The halo concentration will affect the mass loss from stellar encounters in two ways. First, the structural parameters α , β and γ all have explicit dependence on minihalo concentration, which will propagate to the calculation of energy imparted (*i.e.* $\Delta E/E_b \propto \alpha^2(c)/\gamma(c) \sim \ln(c)/c$ when $b \gg b_s$ and $c \gg 1$). Secondly, the response function also has a strong dependence on concentration (see Equation 16), especially when $\Delta E/E_b \gg 1$. Less concentrated minihaloes will become increasingly vulnerable to disruptive stellar encounters. Therefore, it is non-trivial for the semi-analytic model to correctly capture the concentration dependence of minihalo mass loss. In Figure 4, we show the mass loss of minihalo versus minihalo concentration. The best-fit semi-analytic model agrees with the simulation results over a wide range of concentrations, even extrapolating into regimes not covered in our original calibration step above.

3.1.3 Disruption under different minihalo masses

One remaining ingredient of the semi-analytic model that needs to be calibrated is the disruption behavior in the $b \lesssim b_s$ regime. According to Equation 11, the imparted energy will stop rising as b decreases when a characteristic scale b_s is reached. The free, order-unity correction factor is calibrated by simulations. We fix the impact parameter $b = 0.05$ pc and concentration $c = 100$, and run another set of simulations for minihaloes of different masses ranging from 10^{-10} to $10^{-3} M_{\odot}$. In low-mass minihaloes, b_s is small enough that the encounter is in the $b > b_s$ regime, where mass loss is independent of minihalo mass. As minihalo mass increases (and b_s increases), test cases with massive minihaloes enter the $b < b_s$ regime, where stellar disruptions are suppressed. In Figure 5, we show the mass loss as a function of minihalo mass. A transition of the response of the minihalo occurs, and we use the mass of this transition to calibrate

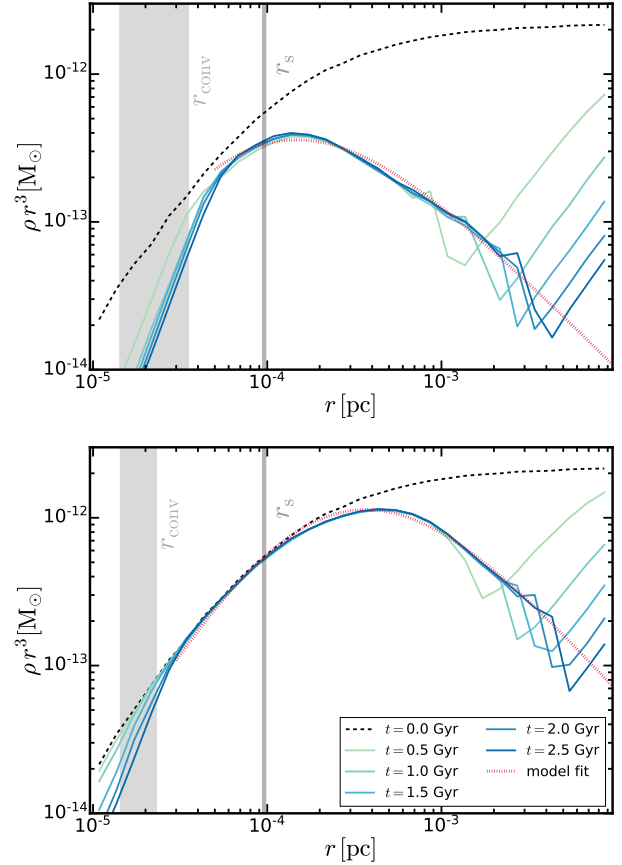


Figure 6. The evolution of minihalo density profiles after a close encounter with a star. For the tests here, the minihalo mass is set as $10^{-10} M_{\odot}$ initialized with the NFW profile at redshift zero, with virial radius $R_{\text{mh}} \sim 0.01$ pc and dynamical time scale $t_{\text{dyn}} \sim 2.2$ Gyr. The halo concentration is $c = 100$. The impact parameter is $b = 2 \times 10^{-5}$ kpc in the top panel and $b = 5 \times 10^{-5}$ kpc in the bottom panel. After the close encounter with the star, the outskirts of the minihaloes are dominantly disrupted in less than a dynamical time. Eventually 81% (60%) of the minihalo mass is disrupted for the $b = 2 \times 10^{-5}$ kpc ($b = 5 \times 10^{-5}$ kpc) case. The density profile of minihalo after disruption can be well-fitted by a broken power-law profile with best-fit asymptotic slopes ($k = 3.2$ for $b = 2 \times 10^{-5}$ kpc, $k = 3.3$ for $b = 5 \times 10^{-5}$ kpc) analogous to that of the Hernquist profile. The “model fit” curve provides an asymptotic limit of the density profile after infinite time. The upturn at the outskirts of the minihalo represents a propagating shell of unbound particles. As this upturn propagates towards the outer part of the minihalo, the density profile gradually converges to the asymptotic limit.

the free parameter to be $f_b = 6$. The predicted mass loss using the best-fit response curve for $c = 100$ haloes is shown in the figure the solid line. In general, the semi-analytic model gives the correct location and shape of the transition at $b \sim b_s$. The mass loss remains a constant at low minihalo masses as indicated by Equation 11 in the $b \gg b_s$ regime. A sharp transition occurs at $b \simeq b_s$ such that the mass-loss rate reduces to almost zero at high minihalo masses.

3.1.4 Density profiles

The density profile will not immediately change after the close encounter with stars, but will gradually relax to the final minihalo profile within a few minihalo dynamical times (Delos 2019). This is mainly because the close encounter with a star occurs on a timescale

much shorter than the minihalo dynamical time. In Figure 6, we show the evolution of minihalo density profiles for minihaloes with mass $10^{-10} M_{\odot}$ and concentration $c = 100$. In the bottom (top) panel, we show the case with impact parameter $b = 2 \times 10^{-5}$ pc (5×10^{-5} pc). The density profile is shown as ρr^3 , which is proportional to $\Delta M / \Delta \log r$, the contribution to total mass per unit logarithmic interval of radius. The vertical shaded region shows the convergence radius for collisionless particles based on the Power et al. (2003) criterion (this is roughly the radius interior to which the numerical two-body relaxation time drops below the Hubble time, a conservative indication of where N-body integration error could be significant). In the $b = 5 \times 10^{-5}$ pc case, the outskirts of the halo are predominantly disrupted while the core of the halo remains relatively unperturbed, leaving approximately 60% of the halo disrupted. Although the central density exhibits a small decrease, its contribution to the total mass loss is negligible and the scale of this decrease is close to the convergence radius of dark matter properties, which makes it hard to distinguish the decrease from a numerical artifact. At the outskirts of the minihalo, the density profile turns up, corresponding to a shell of unbound particles (heated by the encounter) propagating outward. For $b = 2 \times 10^{-5}$ pc, due to higher imparted energy, the disruption is more significant with over 80% disrupted. However, the behavior of the final density profile is rather similar to the previous case.

It is worth noting the remaining minihaloes never relax to a new NFW profile. Instead, the final density profile (after the shell of unbound particles escapes) can be well described by a broken power law of the form

$$\rho(r) = \frac{\rho_0}{\frac{r}{r_0} \left(1 + \frac{r}{r_0}\right)^k}, \quad (18)$$

with the best-fit asymptotic slope $k = 3.2$ for $b = 2 \times 10^{-5}$ kpc and $k = 3.3$ for $b = 5 \times 10^{-5}$ kpc. This slope implies that the density profile is close to a Hernquist (1990) profile ($k = 3$), or in a more general sense, the η -profile family (Dehnen 1993; Tremaine et al. 1994) with an asymptotic slope of -4 . Unsurprisingly, given the scale-free physics involved, this is similar to well-studied simulations of impulsive high-mass ratio galaxy-galaxy encounters (e.g., Hernquist & Quinn 1988; Barnes & Hernquist 1992; Hopkins et al. 2008, 2009; Boylan-Kolchin et al. 2005), particularly the structure of shell galaxies (Hernquist & Quinn 1987; Hernquist & Spergel 1992) and the closely-related slopes of the marginally-bound layer of particles at apocenter in cosmological simulations defined as the halo ‘‘splashback’’ radius (e.g., Diemer & Kravtsov 2014; More et al. 2015). Generically, this slope arises from relaxation after dynamical mass ejection events, which (by definition) excite some material to a broad distribution of energies crossing the specific binding energy $\mathcal{E} = 0$, as the outer slope $k + 1 = 4$ corresponds to the only finite-mass asymptotic power-law distribution function which is continuous through $\mathcal{E} = 0$ (Hernquist et al. 1993).

Therefore, we cannot apply the single-encounter prediction multiple times for an NFW profile in the scenario of multiple encounters. After the first close encounter with stars, the halo profile is no longer well-described by the NFW profile, and the subsequent analysis will be invalid. An alternative but more reasonable approach is to compute the accumulated injected energy ΔE_{tot} for successive encounters and use the response function $\mathcal{F}(\Delta E_{\text{tot}}/E_b)$ to obtain the total mass disruption fraction. And the magnitude of additional disruption from successive encounters is sensitive to the slope of the response function at large $\Delta E_{\text{tot}}/E_b$. This method is reasonable because, in general, minihalo will not have enough time to fully re-

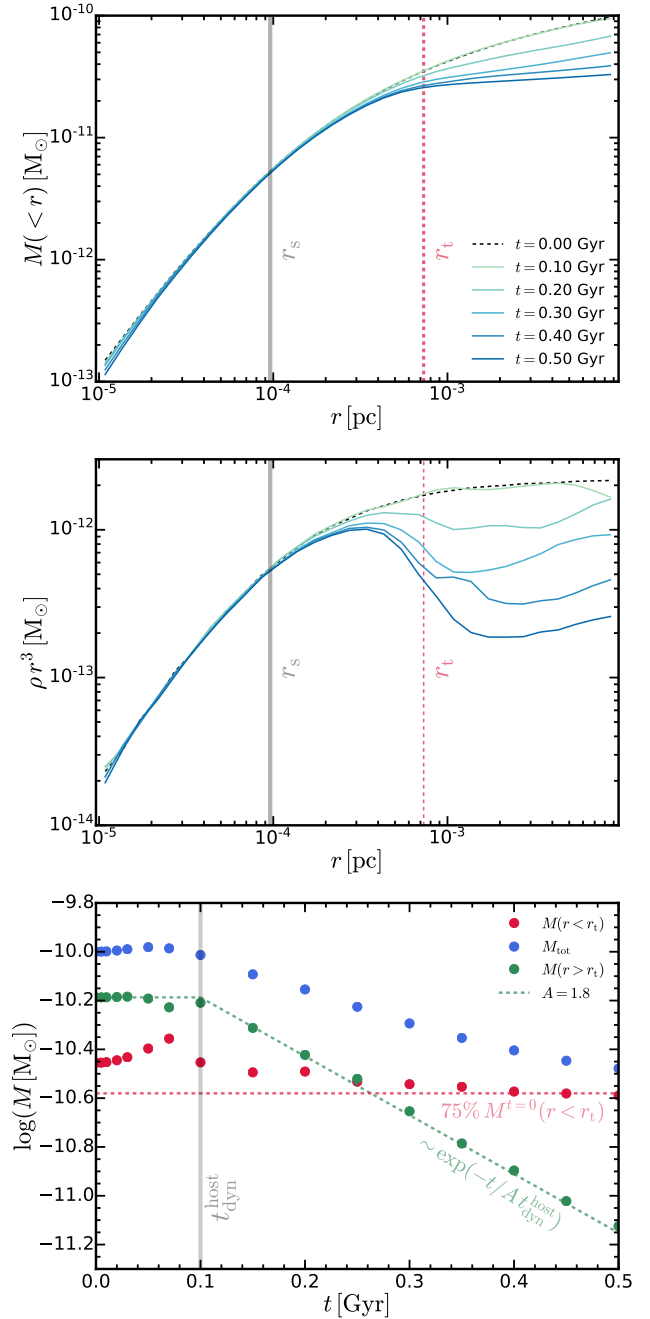


Figure 7. *Top:* The enclosed mass profile of a minihalo with $M = 10^{-10} M_{\odot}$ at $t = 0 - 0.5$ Gyr. The minihalo is on a circular orbit at $R = R_{\odot} = 8$ kpc in a Milky Way-mass dark matter halo. For reference, the dynamical time of the host halo within this radius is about 0.1 Gyr. The gray vertical line indicates the scale radius of the minihalo, and the red vertical dashed line indicates the tidal radius analytically calculated using Equation 13. The mass outside the tidal radius is stripped away at roughly the dynamical time scale of the host halo while the mass inside is marginally perturbed. *Middle:* The density profile of the minihalo at the same time as the top panel. The plot illustrates the behavior of the matter distribution at the outskirts of the minihalo during tidal stripping. *Bottom:* Mass evolution history of the minihalo. The total mass here is the sum of dark matter mass within the initial virial radius of the minihalo. In addition, we show the mass inside and outside the tidal radius as a function of time. After approximately a dynamical time of the host halo, the mass outside the tidal radius starts an exponential decay as described by Equation 14 with the fudge factor $A \approx 1.8$. The mass inside the tidal radius is marginally affected.

lax before the subsequent encounter takes place (for example, the typical time for a minihalo to cross the Milky Way disk given by Equation 19 is much shorter than the dynamical time of the minihalo given by Equation 3). Even in the scenario where the second encounter occurs after minihalo relaxation, the relaxed density profile is effectively more concentrated than the initial NFW profile since the outskirts are dominantly disrupted (as shown in Figure 6) and thus the minihalo becomes less susceptible to subsequent disruptions. In principle, one could recompute the structure parameters as well as the effective concentration number of the relaxed profile and evaluate the disruption fraction of the second encounter. On the other hand, a unique feature of the calibrated response curve is that subsequent encounters with the same energy injection will rapidly become less important. The physical interpretation is that the particles which would be unbound by such an energetic encounter have already been unbound in previous encounters (the loosely bound particles at the outskirts have already be stripped and the remaining particles are more tightly bound and less vulnerable to new encounters). We find that the accumulated injected energy method can reasonably accurately approximate the disruption fraction from the relaxed profile after multiple encounters.

3.2 Simulation of tidal stripping

To validate the semi-analytic description of tidal disruptions of minihaloes in Section 2.2.2, we perform an idealized simulation of a minihalo traveling through the analytic gravitational potential of a Milky Way-mass host halo. The host halo profile is modelled as an NFW profile with mass $M_{\text{vir}} = 10^{12} M_{\odot}$ and concentration $c = 12$ (e.g., Klypin et al. 2002; McMillan 2011; Deason et al. 2012; Bland-Hawthorn & Gerhard 2016). For simplicity, we ignore the baryon content. The minihalo is assumed on a circular orbit with $R = R_{\odot} \simeq 8 \text{ kpc}$. In the top and middle panels of Figure 7, we show the evolution of the enclosed mass profile and density profile of the minihalo. The tidal radius calculated using Equation 13 is shown as the red vertical dashed line. After evolving for about 0.5 Gyr (for reference, the dynamical time scale of the host halo at $R = 8 \text{ kpc}$ is $t_{\text{dyn}}^{\text{host}} \sim 0.1 \text{ Gyr}$, see Equation 15), the enclosed mass profile starts flattening and eventually plateaus outside the analytically evaluated tidal radius. In the bottom panel of Figure 7, we show the mass evolutionary history of this minihalo, and specifically the mass inside and outside the tidal radius. The mass within the tidal radius is almost immune to tidal stripping, with 75% of the mass remaining after 0.5 Gyr. On the other hand, the mass outside the tidal radius exhibits an exponential decay after about $1 t_{\text{dyn}}^{\text{host}}$. The mass loss of the minihalo can be well represented by Equation 14, implying $M(r > r_t) \sim e^{-t/A t_{\text{dyn}}^{\text{host}}}$ with a fudge factor A close to 1.8 for the minihalo tested, in broad agreement with previous numerical studies of more massive CDM subhaloes (e.g., Zentner & Bullock 2003b; Pullen et al. 2014; van den Bosch et al. 2018).

The simulation presented in this section demonstrates that the semi-analytic treatment of tidal disruption works reasonably well in predicting the mass loss and the tidal stripping time scale. Given the fudge factor A found here, the tidal stripping time scale t_{ts} in Equation 15 is at least an order of magnitude smaller than the Hubble time. Therefore, tidal stripping can be treated as an instantaneous process in modelling the cosmological evolution of minihaloes.

4 DISRUPTIONS IN THE REALISTIC MILKY WAY ENVIRONMENT

In the sections above, we described the physical process and consequence of a single stellar encounter and the effects of tidal fields. Next, we will discuss how the impact of successive encounters with an ensemble of stars accumulates and how stellar and tidal disruption affect each other.

4.1 Multiple encounters in the Milky Way disk

Disk stars are the dominant component of the stellar populations in the Milky Way, and thus will be the main contributor to the disruption of dark matter substructures. When a minihalo passes through the stellar disk, it will encounter a slab of stars within a short timescale

$$t_{\text{disk}}^{\times} \simeq 2 \text{ Myr} \left(\frac{H_{\text{d}}}{400 \text{ pc}} \right) \left(\frac{v_{\text{mh}}^{\perp}}{200 \text{ km/s}} \right)^{-1}, \quad (19)$$

where H_{d} is the scale height of the Milky Way thin disk and v_{mh}^{\perp} is the relative velocity of the minihalo perpendicular to the disk plane. Since this disk passage time is much shorter than the dynamical time of dark matter minihaloes, the internal structure of the minihaloes will not have enough time to relax between successive stellar encounters during a single passage. Therefore, a series of encounters with disk stars can be considered effectively as one encounter with the injected energy accumulated over the passage.

4.1.1 Back-of-the-envelope model

First, we will consider a simplified model assuming that a minihalo will be disrupted after a single encounter with an impact parameter smaller than b_{min} given by Equation 12, and it will remain unperturbed if the impact parameter is larger than b_{min} . Note that we aim for a back-of-the-envelope estimate with this simplified model. Consider a minihalo with mass M_{mh} and an average density $\bar{\rho}_{\text{mh}}$, moving through a field of stars with differential number per unit mass $n_{m_*} = dN_*/(dm_* d^3\mathbf{x})$ characterized by the stellar present-day mass function (PDMF), one can choose a normalization such that the total stellar mass density is $\int m_* n_{m_*} dm_* = \rho_*$. We assume that an encounter with impact parameter b has a probability $p = p(b, M_{\text{mh}}, c, m_*, \mathbf{v}, \dots)$ to disrupt the minihalo, where $\mathbf{v} = \mathbf{v}_{\text{mh}} - \mathbf{v}_*$, and that the stars have a locally Maxwell-Boltzmann velocity distribution function with velocity dispersion σ_* which is independent of stellar mass. The disruption rate of the cluster is

$$R = \int d^3\mathbf{v}_* \int 2\pi b db \int dm_* |\mathbf{v}| (dN_*/dm_* d^3\mathbf{x} d^3\mathbf{v}_*) p(b, \bar{\rho}, m_*, \mathbf{v}). \quad (20)$$

Taking the disruption probability p to be a step function between $p = 0$ for $b \gg b_{\text{min}}$ and $p = p_0 \sim 1$ for $b \ll b_{\text{min}}$ as assumed by this simplified model, after the integration, we obtain

$$R = \left(\frac{\pi \alpha^2 (c) G}{\gamma(c) \bar{\rho}_{\text{mh}}} \right)^{1/2} \rho_*. \quad (21)$$

Integrating this over time for a given minihalo gives a survival fraction $f_{\text{survive}} = \exp(-\tau)$ where $\tau \equiv \int R dt = \int R d\ell / v_{\text{mh}}$ along the minihalo trajectory. The time-integrated destruction probability τ is dominated by the minihalo time in the disk. If a minihalo stayed in

the disk over the entire Hubble time, then

$$\begin{aligned} \tau &= \left(\frac{\pi \alpha^2(c) G}{\gamma(c) \bar{\rho}_{\text{mh}}} \right)^{1/2} \rho_* \frac{1}{H_0} \\ &\sim 2.2 \times 10^4 \left(\frac{\langle \rho_{*, \text{disk}} \rangle}{1 \text{ M}_\odot / \text{pc}^3} \right) \left(\frac{c}{100} \right)^{-1/2} \left(\frac{1+z_i}{3} \right)^{-3/2}, \end{aligned} \quad (22)$$

where we use the asymptotic approximation $\alpha^2(c)/\gamma(c) \sim 1/c$ at large c . This implies the complete disruption of the minihalo if it is always in the disk. On the other hand, if a minihalo only has a single passage through the disk, then

$$\begin{aligned} \tau_{\text{single}} &= \int R \, dt \\ &\simeq \left(\frac{\pi \alpha^2 G}{\gamma \bar{\rho}_{\text{mh}}} \right)^{1/2} \int \rho_* \, dh / v_{\text{mh}}^\perp \\ &\sim 0.5 \left(\frac{c}{100} \right)^{-1/2} \left(\frac{1+z_i}{3} \right)^{-3/2} \left(\frac{\Sigma_*}{70 \text{ M}_\odot \text{ pc}^{-2}} \right) \left(\frac{v_{\text{mh}}^\perp}{200 \text{ km s}^{-1}} \right)^{-1}, \end{aligned} \quad (23)$$

where Σ_* is the stellar surface density of the Milky Way disk, which is reasonably well-fit by an exponential profile $\Sigma_* \approx \Sigma_0 \exp(-R/R_d)$ with $\Sigma_0 = 816.6 \text{ M}_\odot \text{ pc}^{-2}$ and $R_d = 2.9 \text{ kpc}$ ($\Sigma_0 = 209.5 \text{ M}_\odot \text{ pc}^{-2}$ and $R_d = 3.31 \text{ kpc}$) for the thin (thick) disk of the Milky Way (e.g., [McMillan 2011, 2017](#)). If we are only interested in the Solar neighborhood ($R_\odot \approx 8 \text{ kpc}$, see [Bland-Hawthorn & Gerhard 2016](#) for a review of measurements on R_\odot), the total surface density of both the thin and thick disks is $\Sigma_*^\odot \sim 70 \text{ M}_\odot \text{ pc}^{-2}$. Therefore, the impact of a single passage through the disk is insignificant for reasonably high halo concentrations.

Besides the two extreme cases above, the more realistic scenario is successive passages through the disk, where the number of passages of a minihalo through the disk is a critical factor. Assuming circular orbits, the number of disk passages for minihaloes in the Solar neighborhood is approximately $T_{\text{Hubble}}/T_{\text{circ}} \sim 60$, leading to an $O(1)$ effect. Therefore, those minihaloes in the Solar neighborhood should experience significant disruption. To make a quantitative prediction for the remaining mass and structure of minihaloes, we need a more complete model, which will be described in the following.

4.1.2 General response model

In general, the mass loss of minihaloes in single (or multiple successive) encounters characterized by the response curve $1 - \Delta M_{\text{mh}}/M_{\text{mh}} = \mathcal{F}(\Delta E_{\text{tot}}/E_b, c)$ was found in Section 3. Assuming the surface density of stars in the disk is large enough so that we can neglect stellar shot noise (discussed further below), the total energy injection $\Delta E_{\text{tot}}/E_b$ when crossing a localized slab of stars can be calculated by integrating over all possible impact parameters,

masses and velocities of stars

$$\begin{aligned} \frac{\Delta E_{\text{tot}}}{E_b} &= \int d^3 \mathbf{v}_* \int d\ell \int 2\pi b \, db \int dm_* \\ &\quad (dN_*/dm_* d^3 \mathbf{x} d^3 \mathbf{v}_*) \frac{\Delta E}{E_b} \\ &= G \int d\ell \int d^3 \mathbf{v}_* f(\mathbf{v}_*) \frac{1}{|\mathbf{v}_* - \mathbf{v}_{\text{mh}}|^2} \int dm_* n_{m_*} m_*^2 \\ &\quad \times \left(\int_{b_s}^\infty \frac{\alpha^2(c)}{\pi \gamma(c) \bar{\rho}_{\text{mh}}} \frac{2\pi b \, db}{b^4} + \int_0^{b_s} \frac{\alpha^2(c)}{\pi \gamma(c) \bar{\rho}_{\text{mh}}} \frac{2\pi b \, db}{b_s^4} \right) \\ &\simeq \frac{G m_\kappa \Sigma_*}{\sigma_*^2 + v_{\text{mh}}^2} \frac{2 \alpha^2(c)}{\gamma(c) \bar{\rho}_{\text{mh}} b_s^2}, \end{aligned} \quad (24)$$

where $\Delta E/E_b$ is evaluated using Equation 11, σ_* is the *one-dimensional* velocity dispersion of stars and $f(\mathbf{v}_*)$ is the Maxwell-Boltzmann velocity distribution function⁸. m_κ is a characteristic mass that depends on the PDMF of stars in the Milky Way,

$$m_\kappa \rho_* = \int dm_* n_{m_*} m_*^2. \quad (25)$$

A simple approximation which gives a good fit to the Milky Way data is to take the Kroupa IMF ([Kroupa 2001](#)) as the PDMF at $M_* \leq 1 \text{ M}_\odot$ (since the evolutionary effects are small at low masses) with a power-law cutoff $n_{m_*} \sim m_*^{-4.5}$ at $M_* > 1 \text{ M}_\odot$ (e.g., [Scalo 1986; Kroupa et al. 1993; Sollima 2019](#)). After the integration, we obtain $m_\kappa \approx 0.6 \text{ M}_\odot$, which is insensitive to the minimum or maximum star mass assumed. m_κ can be viewed as the characteristic mass of the most effective disruptor, which can vary in different environments. For example, a clumpy medium may have significantly higher m_κ and thus stronger disruption effects. The integration in Equation 24 is carried out to infinite distances, where in principle the localized quantities we define in a disk patch no longer apply. This will not affect the results significantly since the contribution from distant stars is suppressed by the $1/b^4$ dependence of energy imparted.

It is, however, still important to note that Equation 24 will no longer be valid if the stellar surface density is small enough that shot noise becomes important, *i.e.* when $\pi b_c^2 \Sigma_*/m_\kappa \sim 1$. If we take $m_\kappa = 0.6 \text{ M}_\odot$ as estimated above, we obtain the cut-off impact parameter as

$$b_c = 0.044 \text{ pc} \left(\frac{m_\kappa}{0.6 \text{ M}_\odot} \right)^{1/2} \left(\frac{\Sigma_*}{100 \text{ M}_\odot / \text{pc}^2} \right)^{-1/2}. \quad (26)$$

If shot noise becomes dominant, $b_c \gg b_s$, the total energy injection becomes⁹

$$\frac{\Delta E_{\text{tot}}}{E_b} = \frac{G m_\kappa \Sigma_*}{\sigma_*^2 + v_{\text{mh}}^2} \frac{\alpha^2(c)}{\gamma(c) \bar{\rho}_{\text{mh}} b_c^2}. \quad (27)$$

Connecting the behavior at $b_c \ll b_s$, the general solution of the

⁸ The integral in the velocity space is evaluated in the $v_{\text{mh}} \gg \sigma_*$ or $v_{\text{mh}} \ll \sigma_*$ regime first. The leading order term in the asymptotic limits can be connected using the expression, $1/(\sigma_*^2 + v_{\text{mh}}^2)$. The relative error between this expression and the true result is suppressed by the factor $(\sigma_*/v_{\text{mh}})^2$ when $v_{\text{mh}} \gg \sigma_*$ and vice versa.

⁹ More accurately, we can calculate b_c at each value of the stellar mass m_* , using the same PDMF and $\pi b_c^2(m_*) dN_*(> m_*)/d\text{Area} = 1$, insert this into Equation 24, and then integrate over all masses numerically to define an appropriately-weighted b_c . Doing so, we find that this gives an “effective” b_c which is only $\sim 8\%$ larger than what we obtain using $\pi b_c \Sigma_*/m_\kappa = 1$.

accumulated energy injection during one disk passage can be written as

$$\frac{\Delta E_{\text{tot}}}{E_b} = \frac{G m_\kappa \Sigma_*}{\sigma_*^2 + v_{\text{mh}}^2} \frac{\alpha^2(c)}{\gamma(c) \bar{\rho}_{\text{mh}}} \frac{2}{b_s^2 + 2b_c^2} \quad (28)$$

Typically, $b_s > b_c$ for massive minihaloes with low concentrations and $b_s < b_c$ for low-mass minihaloes with high concentrations. It is also worth noting that m_κ will cancel out when $b_c \gg b_s$, implying that clumpiness of the medium only matters for minihaloes with physical sizes comparable to or larger than the typical spacing of the disruptors.

When the Galactic disk is dominated by stars, our treatment by integrating the cumulative perturbations from disk stars to large distances (rather than considering only close encounters like in the back-of-the-envelope model) should be physically equivalent to the disk shocking effect (e.g., Ostriker et al. 1972; Binney & Tremaine 1987; Gnedin et al. 1999; Stref & Lavalley 2017) studied in the depletion of substructures in the Milky Way (e.g., D’Onghia et al. 2010; Stref & Lavalley 2017; Facchinetti et al. 2022). The disk shocking calculation implies (e.g., Binney & Tremaine 1987; Stref & Lavalley 2017)

$$\frac{\Delta E_{\text{tot}}}{E_b} \propto \frac{R_{\text{mh}}^2 g_{z,\text{disk}}^2}{\sigma_{\text{mh}}^2 v_{\text{mh}}^2} \propto \frac{R_{\text{mh}}^2 \Sigma_{\text{disk}}^2}{M_{\text{mh}}/R_{\text{mh}} v_{\text{mh}}^2} \propto \frac{\Sigma_*^2}{v_{\text{mh}}^2 \bar{\rho}_{\text{mh}}}, \quad (29)$$

where $g_{z,\text{disk}} \propto \Sigma_{\text{disk}} \approx \Sigma_*$ is the gravitational acceleration at disk vicinity, σ_{mh} is the internal velocity dispersion of the minihalo which should scale as $\sqrt{G M_{\text{mh}}/R_{\text{mh}}}$. However, taking our Equation 28 to a “smooth” disk limit (m_κ being infinitesimal), we do not get the disk shocking limit naturally. The key difference is that we assume that all individual stellar encounter events are independent. We evaluate the energy injection in each independent event first before summing up, while the disk shocking evaluates the tidal field of the entire baryonic disk simultaneously before estimating the momentum and energy injection. This independence assumption we made is supported by the fact that the disk scale height, $H \sim O(100)$ pc, is at least two orders of magnitude larger than the characteristic impact parameter $b_s \sim R_{\text{mh}}$ of the minihalo, so individual encounters should operate locally in an independent fashion. If we abandon the independence assumption, the break in energy injection at b_s in Equation 7 (which comes from resolving individual encounters) will disappear. We can integrate the $1/b^4$ law until reaching b_c and would obtain

$$\frac{\Delta E_{\text{tot}}}{E_b} \propto \frac{m_\kappa \Sigma_*}{v_{\text{mh}}^2 \bar{\rho}_{\text{mh}} b_c^2} \propto \frac{\Sigma_*^2}{v_{\text{mh}}^2 \bar{\rho}_{\text{mh}}}, \quad (30)$$

which is totally consistent with the disk shocking calculation.

Depending on the orbit of the minihalo, it can pass through the stellar disk multiple times after falling into the host. When the orbital time is much smaller than the relaxation time of the minihalo, the combined effect can again be modelled as one single passage with the accumulated injected energy. The total number of passages and stellar surface densities at the encounter point should take an ensemble average of all possible stellar orbits passing the location of the detector. In Appendix C, we calculate the relevant correction factors from the ensemble average of all possible orbits with a simplified model. The accumulated injected energy will ultimately be fed to the response function $\mathcal{F}(\Sigma \Delta E_{\text{tot}}/E_b)$ to calculate the mass loss. If the time between passages is comparable to the minihalo relaxation time, the density profile of minihaloes can be relaxed to the asymptotic profile shown in Figure 6. However, as discussed in Section 3.1.4, we can still use the accumulated injected energy and the response curve to approximate the disruption fraction. The slope

of the response function in Figure 3 at high $\Delta E/E_b$ suggests that a much larger injected energy does not necessarily correspond to a much more significant disruption, which is expected as the remaining core of the minihalo is less sensitive to subsequent disruption events.

4.2 Semi-analytic model to combine stellar and tidal disruptions

As the minihalo moves closer to the Galactic center, both r_t (Equation 13) and $t_{\text{ts}}(R)$ (Equation 15) will decrease sharply. Therefore, the total mass loss of an infalling minihalo is dominated by its pericenter passages. For minihaloes of interest for detection (e.g. in the Solar neighborhood $R_\odot \approx 8$ kpc), the tidal-stripping time scale during a pericenter passage at R_\odot is $O(100)$ Myr, which is much shorter than the lifetime of the minihalo in the host ($\sim T_{\text{Hubble}}$). We assume that the mass of an infalling minihalo outside the tidal radius will be quickly stripped away during the first few pericenter passages before the impact of stellar disruptions start to accumulate.

For simplicity, we evaluate the tidal radius at the target radius r_{obs} of observation, assuming a circular orbit

$$r_t = r_{\text{obs}} \left[\frac{M_{\text{mh}}(r < r_t)/M_{\text{MW}}(r < r_{\text{obs}})}{3 - \left. \frac{d \ln M_{\text{MW}}}{d \ln R} \right|_{r_{\text{obs}}}} \right]^{1/3}. \quad (31)$$

where the Milky Way halo mass distribution is modelled as an NFW profile for dark matter plus a Hernquist profile (Hernquist 1990) for the stellar content

$$M_{\text{MW}}(< r) = M_{\text{dm}} \frac{f^{\text{NFW}}(r/r_s)}{f^{\text{NFW}}(c)} + M_b \frac{r^2}{r^2 + a^2}, \quad (32)$$

where $f^{\text{NFW}}(x) \equiv \ln(1+x) - x/(1+x)$, the host halo parameters are $c = 12$, $M_{\text{dm}} = 10^{12} M_\odot$ (e.g., Klypin et al. 2002; McMillan 2011; Deason et al. 2012; Bland-Hawthorn & Gerhard 2016). For baryon properties, abundance-matching studies have shown that a Milky-Way mass system typically has a stellar-to-total-mass ratio of $M_b \approx 0.01 M_{\text{dm}}$ (e.g., Moster et al. 2013) and the half mass radius $r_{1/2}^* \approx 0.02 R_{\text{vir}}$ (e.g., Somerville et al. 2018). The scale radius of the Hernquist profile is related to the stellar-half-mass-radius as $a = 0.414 r_{1/2}^*$ (Hernquist 1990).

The post-stripping density profile of the minihalo is assumed to be a truncated NFW profile at r_t , which is equivalent to a normal NFW profile with effective virial radius, concentration, and overdensity as

$$\begin{aligned} R_{\text{vir}}^{\text{eff}} &= r_t, \\ c_{\text{eff}} &= c \frac{r_t}{R_{\text{vir}}}, \\ \Delta_{\text{eff}} &= \frac{\log(1+c_{\text{eff}}) - c_{\text{eff}}/(1+c_{\text{eff}})}{\log(1+c) - c/(1+c)} \frac{c^3}{c_{\text{eff}}^3} \Delta_c, \end{aligned} \quad (33)$$

The mass loss due to the tidal disruption is

$$1 - \Delta M_{\text{mh}}/M_{\text{mh}} = \frac{\log(1+c_{\text{eff}}) - c_{\text{eff}}/(1+c_{\text{eff}})}{\log(1+c) - c/(1+c)}. \quad (34)$$

We assume that the tidal stripping happens before the minihalo settles to its current-day bound orbit to the host and before any stellar encounters. The stripped minihalo forms the initial condition for the following stellar disruptions. Therefore, for a minihalo observed at r_{obs} , the energy accumulated from stellar encounters can be written as (following Equation 28 but considering multiple passages through

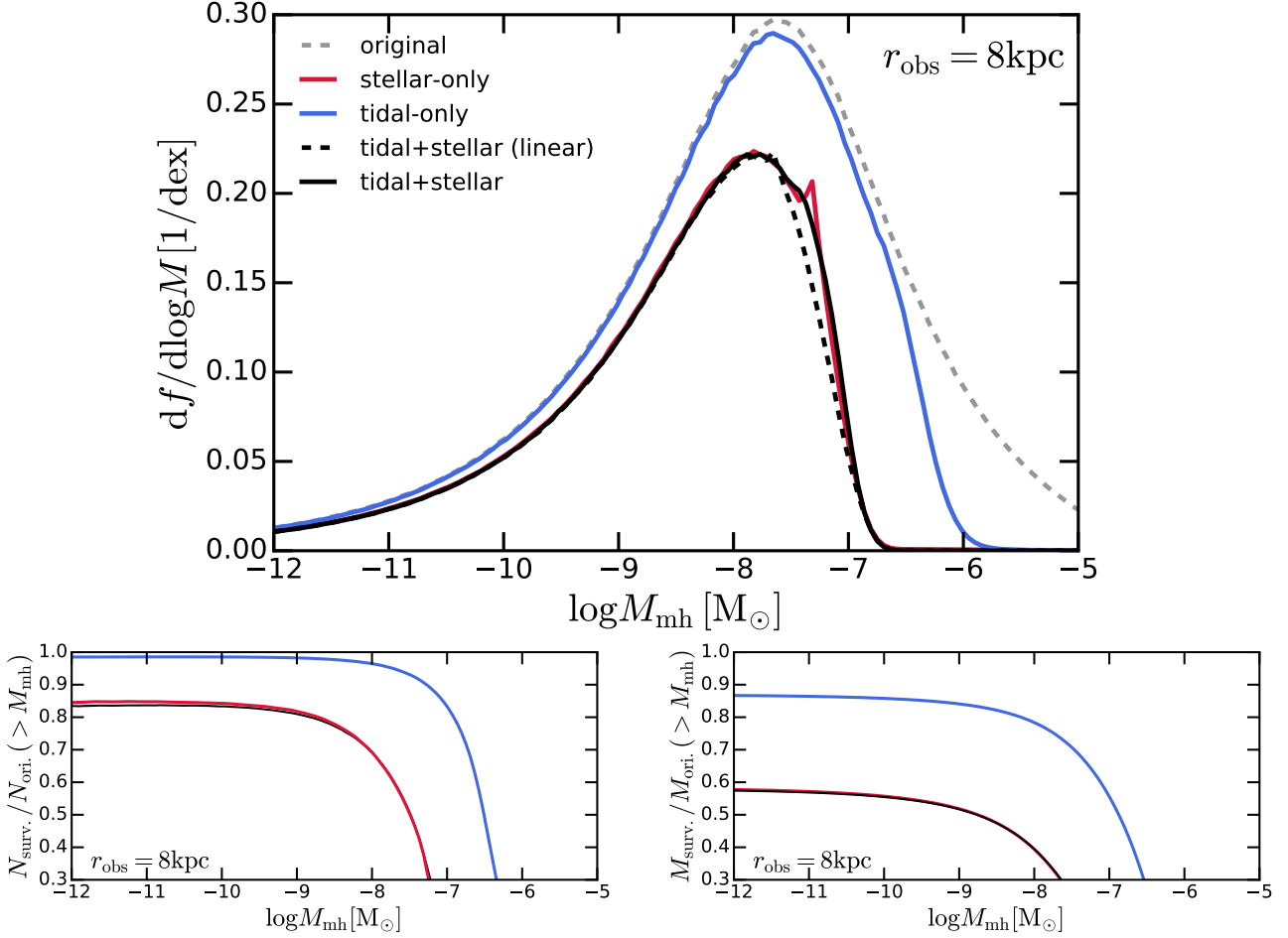


Figure 8. *Top:* Mass function of minihaloes (from axion miniclusters) at the Solar neighborhood ($r_{\text{obs}} \approx 8\text{kpc}$). We assume that AMC model with $m_a = 25 \mu\text{eV}$. The mass function before disruption is shown as the gray dashed line. The mass function after processing only tidal (or stellar) disruption is shown as the blue (red) solid line. The mass function post-disruption, combining both tidal and stellar disruption, is shown as the solid black line. The mass function post-disruption, combining tidal and stellar disruption linearly, is shown as the dashed black line. In general, the disruptions taken together induce approximately a 30% decrease in the peak value of the mass function and shift the mass of the peak by roughly half an order of magnitude. The massive end is more strongly affected by disruption than the low-mass end. *Bottom:* We show the integrated number (left) and mass (right) of minihaloes before and after disruption. The typical survival fraction of minihaloes with $M_{\text{mh}} \geq 10^{-12} M_{\odot}$ is 83% in terms of number and about 58% in terms of mass. Stellar disruption is the dominant disruption mechanism through the entire mass range of interest in this case.

the disk during the lifetime of the minihalo)

$$\frac{\Delta E_{\text{tot}}}{E_b}(r_{\text{obs}}) = \left\langle N_p \left\langle \frac{G m_{\kappa} \Sigma_*}{\sigma_*^2 + v_{\text{mh}}^2} \frac{\alpha^2 (c_{\text{eff}})}{\gamma (c_{\text{eff}}) \Delta_{\text{eff}} \rho_{\text{crit}}(z_i)} \frac{2}{b_s^2 (c_{\text{eff}}, R_{\text{vir}}^{\text{eff}}) + 2b_c^2(\Sigma_*)} \right\rangle_x \right\rangle_0$$

$$= \overline{N_p} f_{\theta} f_{\Sigma_*} \frac{G m_{\kappa} \Sigma_*(r_{\text{obs}})}{\sigma_*^2 + v_{\text{mh}}^2} \frac{\alpha^2 (c_{\text{eff}})}{\gamma (c_{\text{eff}}) \Delta_{\text{eff}} \rho_{\text{crit}}(z_i)} \frac{2}{b_s^2 (c_{\text{eff}}, R_{\text{vir}}^{\text{eff}}) + 2b_c^2(\Sigma_*(r_{\text{obs}}))},$$

$$\overline{N_p} = f_{N_p} N_p^{\text{circ}}, \quad N_p^{\text{circ}} = 2 T_{\text{Hubble}} / T_{\text{circ}}(r_{\text{obs}}) \quad (35)$$

where N_p is the number of passages through the stellar disk, $\langle \rangle_0$ denotes averaging over an ensemble of minihaloes observed at r_{obs} with all possible orbits. Therefore, $\overline{N_p}$ represents the averaged number of passages over all possible orbits. N_p^{circ} is the number of passages assuming the minihalo is on a circular orbit with radius r_{obs} calcu-

lated based on the Hubble time T_{Hubble} and the circular orbit period $T_{\text{circ}}(r_{\text{obs}})$. f_{N_p} characterizes the deviation of $\overline{N_p}$ from this circular orbit estimation. In Equation 35, Σ_* is the stellar surface density where the minihalo crossed the disk (the surface density profile $\Sigma_*(r)$ is given below Equation 23). $\langle \rangle_x$ denotes averaging over all past disk crossings given the orbit of the minihalo. The correction factor f_{Σ_*} characterizes the deviation of the averaged Σ_* at all past encounter locations for all possible orbits from $\Sigma_*(r_{\text{obs}})$. f_{θ} accounts for the increased effective stellar surface density when the minihalo is not passing perpendicular to the disk, see Appendix C for details). In Appendix C, f_{N_p} and f_{Σ_*} are estimated based on the orbital model of an isothermal halo. The combined effect of f_{θ} , f_{N_p} and f_{Σ_*} on $\Delta E_{\text{tot}}/E_b$ is $\mathcal{O}(10)$ at the Solar neighborhood. The velocity term $\sigma_*^2 + v_{\text{mh}}^2$ has weak dependence on r_{obs} and minihalo orbits, so it is assumed to be the constant value $(250 \text{ km/s})^2$ for simplicity.

We note that b_c has an implicit dependence on the surface density at the encounter. When $b_c \gg b_s$ (when Σ_* is large or M_{mh} is small), $\Delta E_{\text{tot}}/E_b$ will be proportional to Σ_*^2 and the correction factor f_{Σ_*}

should be replaced with $f_{\Sigma_*^2}$ (see the calculation in Appendix C). To properly account for this, we model the transition from f_{Σ_*} to $f_{\Sigma_*^2}$ empirically as

$$f = f_{\Sigma_*} + (f_{\Sigma_*^2} - f_{\Sigma_*}) \frac{1}{1 + e^{-k \log(\sqrt{2}b_c/b_s)}} \quad (36)$$

where $k = 3$ is assumed. We note that the value of k or the detailed form of the transition does not affect the post-disruption mass function in any significant way.

4.3 Monte Carlo sampling of the minihaloes

We are ready to implement all the physics of disruption discussed above to a sample of minihaloes and track their mass loss. We model the evolution of the minihalo population in the Milky Way halo following the steps below:

- We initialized a Monte Carlo sample of minihaloes. First, we construct a grid of infall redshifts from $z_i^{\min} = 0$ to $z_i^{\max} = 150$ (uniform in $\log(1 + z_i)$), and compute the infall probability at each redshift point as $\Delta f_{\text{col}}^{\text{CDM}}(z_i)$ (using the matter power spectrum from adiabatic CDM fluctuations on small scales, see the discussion in Section 2.1). Then, at each redshift point, the minihalo masses are sampled uniformly over the dynamical range 10^{-14} to $10^{-3} M_\odot$. The number densities of these minihaloes are calculated following the redshift-dependent pre-infall mass function given in Section 2.1 and Appendix A. The weight of each individually sampled minihalo is proportional to the product of the number density and the infall probability at z_i . The minihalo concentrations are calculated following the mass-concentration relation given in Section 2.1. These sampled physical properties represent the initial status of the minihaloes upon falling into the Milky Way host.

- Tidal stripping and structural corrections are applied to the sampled minihaloes as described in Equation 33 and 34. Since the r_t solved from Equation 31 after normalizing over r_s is independent of minihalo mass, we calculate r_t/r_s on a grid of c and z_i for several different choices of r_{obs} and prepare them as lookup tables for efficient interpolation of the tidal radius.

- After the tidal stripping and the implementation of relevant structural corrections, we apply the stellar disruption with the mass loss given by $\mathcal{F}(\Delta E_{\text{tot}}/E_b, c)$. The cumulative energy injection from stellar encounters, $\Delta E_{\text{tot}}/E_b$, is evaluated with Equation 35 using the structural parameters corrected after tidal disruptions. We include the orbit corrections derived in Appendix C.

All the results demonstrated below have passed the convergence tests over hyperparameters in the sampling approach above, including the maximum sample redshift z_i^{\max} , the mass range of sampling, the number of redshift grid points, the number of samples at each redshift and the resolution of tidal correction grid.

5 RESULTS

5.1 Post-disruption mass functions

In Figure 8, we show the mass function of minihaloes (from AMC with the fiducial $m_a = 25 \mu\text{eV}$ as an example) at the Solar neighborhood ($r_{\text{obs}} = 8 \text{ kpc}$). The mass functions are presented as the matter mass fraction (with respect to the total dark matter mass) in minihaloes per unit logarithm interval (dex) of minihalo mass. We have assumed the axion gives the correct dark matter relic abundance. We present the initial (pre-disruption) mass function, the post-tidal/stellar disruption mass function, the mass function considering

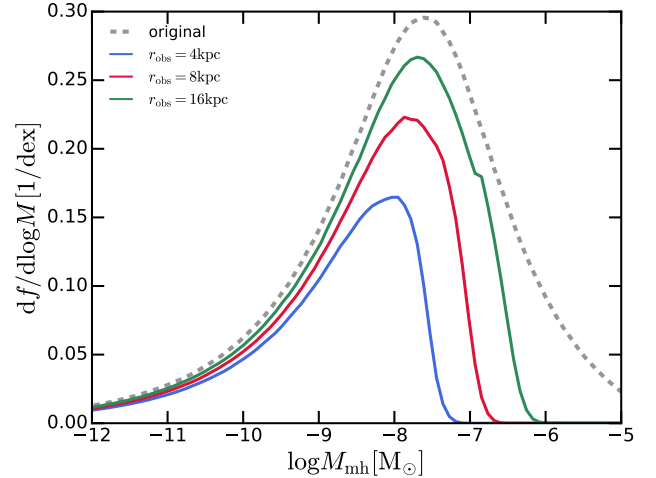


Figure 9. Mass function of minihaloes (from AMC with $m_a = 25 \mu\text{eV}$) observed at three galactocentric distances ($r_{\text{obs}} = 4, 8, 16 \text{ kpc}$). A similar reduction pattern in the mass density of minihaloes is found at each distance, with stronger disruption at smaller radii and the massive end of the mass function. Stellar disruption is the dominant disruption mechanism at all radii.

the combined effect of tidal and stellar disruptions, and the mass function aggregating tidal and stellar disruptions linearly. With both tidal and stellar disruption, the peak of the mass function is reduced by about 30% accompanied by roughly half an order of magnitude mass shift of the peak. The low-mass end of minihaloes is less disrupted than the massive end because lighter minihaloes generically form earlier in these models and are more concentrated. Comparing the two disruption mechanisms, the stellar disruption dominates over the entire mass range, which agrees with the conclusion of previous studies of AMC (e.g., Kavanagh et al. 2020; Lee et al. 2021a). It is worth noting that tidal disruption can alter the structural parameters and enhance the average density of minihaloes, which could lead to non-linear effects on the following stellar disruption. However, in our experiments, the effect is relatively weak. We note that a spike shows up in the post-disruption mass function at $\log M_{\text{mh}} \sim -7$ when considering only the stellar disruption. The spike is related to a turnover in the distribution of the minihalo initial concentrations and will be discussed in the following section. In the bottom panels of Figure 8, we show the integrated fraction of disrupted minihaloes in number and total mass, respectively. The overall survival fraction of minihaloes with $M_{\text{mh}} \geq 10^{-12} M_\odot$ is about 83% in terms of number and about 58% in terms of mass. The survival fraction will quickly diminish to $\leq 30\%$ at $M_{\text{mh}} \geq 10^{-7} M_\odot$. Again the dominance of the stellar disruption is manifest.

In Figure 9, we show the post-disruption mass function of minihaloes at different galactocentric distances, $r_{\text{obs}} = 4, 8, 16 \text{ kpc}$, for the $m_a = 25 \mu\text{eV}$ AMC model. We find similar behaviour of the post-disruption mass functions at different target radii. In all cases, the massive end is more severely disrupted, and stellar disruption dominates. The disruption at smaller galactocentric distances is stronger primarily due to enhanced stellar surface densities. The geometric assumptions of our model will break at the central bulge ($r_{\text{obs}} \lesssim 1 \text{ kpc}$) of the galaxy. The effective stellar density can be much higher than implied by the disk model, and minihaloes will spend most of their lifetime in dense stellar environments. According to the back-of-the-envelope estimation given in Equation 22, the survival probability

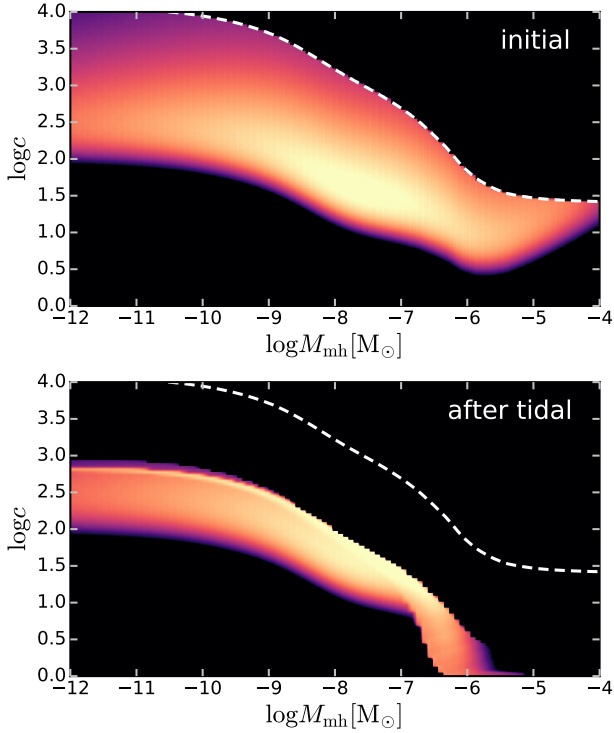


Figure 10. *Top:* Mass distribution of sampled minihaloes in the phase space (c versus M_{mh}) before disruption. The mass concentration relation from Lee et al. (2021a) is shown with the white dashed line (assuming $z_i = 0$). The down scatter of concentration on this plane is driven by the spread of the minihalo infall redshift, z_i . The scatter shrinks to zero towards the massive end, since most of the massive minihaloes have $z_i \sim 0$. *Bottom:* Mass distribution of sampled minihaloes in the phase space after tidal disruption. Effectively, tidal disruption lowers the concentration of minihaloes to r_t/r_s while increasing the averaged densities of minihaloes (since the low-density outskirts have been shredded). The effect is significant in massive, low-concentration minihaloes.

in this scenario should diminish to zero with moderately high stellar densities.

5.2 Impacts of different disruption mechanisms

To better illustrate the impact of tidal disruption, in the top panels of Figure 10, we show the mass distribution of minihaloes on the plane of c versus M_{mh} before and after the tidal disruption. The initial mass concentration relation has a big scatter driven by the distribution of z_i . At the massive end, the scatter approaches zero since all of the minihaloes there have $z_i \sim z_c \sim 0$. Tidal disruptions (along with corrections on minihalo structural parameters, see Equation 33) effectively lower the concentration of minihaloes, especially at the massive end. We need to note that the average densities of minihaloes are enhanced in the meantime, so the net effects over following stellar disruptions will depend on the trade-off between lowered concentrations and enhanced densities (see Equation 35).

In Figure 11, we show the mass loss versus the initial mass of minihalo decomposed by the disruption mechanism. The stellar disruption is the dominant mechanism over the entire mass range of interest. However, the tidal disruptions do have non-linear effects in modifying the structural parameters of minihaloes prior to stellar encounters. The net effect over stellar disruptions is a trade-off between lowered effective concentrations and enhanced average densities of minihaloes. It suppresses (promotes) the stellar disruption

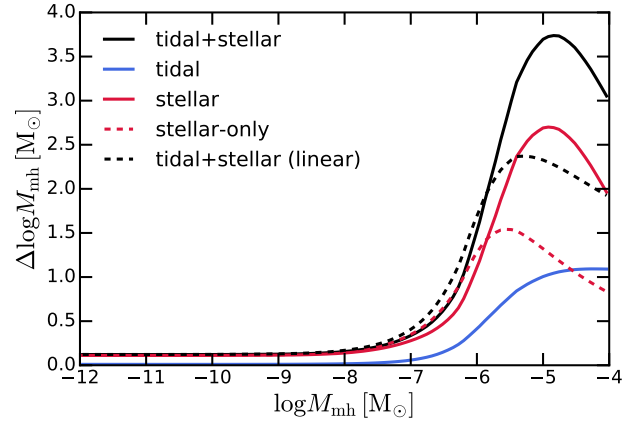


Figure 11. Mass loss induced by disruption versus the initial mass of minihaloes. We have decomposed the mass loss to tidal and stellar disruptions. The red dashed line shows the mass loss due to stellar disruption when there are no prior tidal corrections. The black dashed line shows the total mass loss if adding stellar and tidal terms linearly. In all cases, stellar disruption is the dominant mechanism. The non-linear effects of tidal disruption suppress stellar disruption at $\log M_{\text{mh}} < -6$, but promote that at $\log M_{\text{mh}} > -6$. Nevertheless, this does not affect the mass functions shown in Figure 8, since the differences show up at the mass where the density of minihaloes is dropping rapidly.

at $\log M_{\text{mh}} < -6$ ($\log M_{\text{mh}} > -6$). Nevertheless, the non-linear effects do not affect much the mass functions or the overall survival probability of minihaloes shown in Figure 8 since most of the differences show up at the decreasing edge of the mass function. Another interesting feature to note is the peak of the mass loss curve due to stellar disruptions at around $\log M_{\text{mh}} \sim -5$ (-6 if tidal disruption is not introduced). The peak is related to the turnover feature (at the same mass scale) of the mass-concentration distribution shown in the upper panel of Figure 10. The peak in the mass loss curve corresponds to the spike in the minihaloes mass function (stellar-only case) shown in Figure 8. This is an example that convolution of the mass-concentration relation and mass function gives rise to non-linear features.

5.3 Disruption for different physics models

Here we explore the disruption of minihaloes in different physics models summarized in Section 2.1. These models feature different initial mass functions and mass-concentration relations.

In the top panel of Figure 12, we present the pre- and post-disruption mass functions of minihaloes in the AMC model with axion mass $m_a = 1.25, 25, 500 \mu\text{eV}$. For the EMD case, we show the model with reheating temperature $T_{\text{rh}} = 15, 30, 60 \text{ MeV}$. The numeric sampling experiments are all conducted at $r_{\text{obs}} = 8 \text{ kpc}$. Since both the initial mass functions and mass-concentration relations are almost self-similar with a horizontal mass shift (and the relative mass change only depends on c and ρ_{mh}), the post-disruption mass functions are also similar albeit with a horizontal shift. The minihalo abundance reduction from disruptions has similar patterns between the AMC and EMD models. In the bottom panel of Figure 12, we show the mass survival fraction of minihaloes. Regardless of the model choice, the overall survival fraction is about 60% for minihaloes with $M_{\text{mh}} > 10^{-12} M_{\odot}$. It is visible that the AMC (EMD) model with higher m_a (T_{rh}) suffers from stronger disruption at the massive end. This is due to the lower minihalo concentration at the

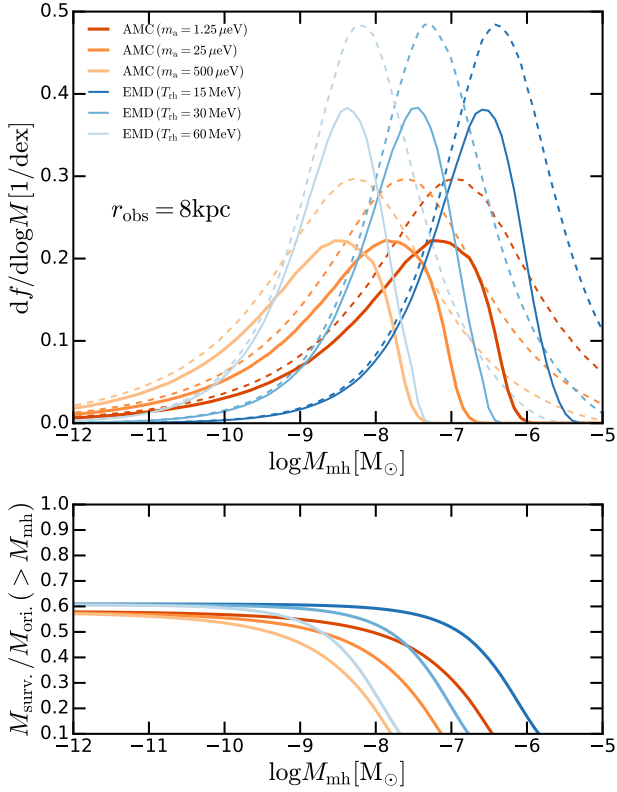


Figure 12. *Top:* Mass function of minihaloes in different models before (dashed) and after (solid) disruption. Two different models are studied: post-inflationary AMCs and EMD. The reheating temperature for the EMD era is $T_{\text{rh}} = 15, 30, 60 \text{ GeV}$ while the axion mass in the post-inflationary AMC scenario is chosen as $m_a = 1.25, 25, 500 \mu\text{eV}$. These parameters are purely chosen for illustrative purposes (especially for the EMD model), and one can use other parameters which will shift the mass range, but the shape of the mass function will remain the same. *Bottom:* The integrated mass survival fraction of minihaloes for the models shown in the top panel. Regardless of the model choices, the overall survival fraction of minihaloes with $M_{\text{mh}} > 10^{-12} M_{\odot}$ is around 70%.

same mass in these models (as shown in Figure 1). The EMD models exhibit sharper decreases in survival fraction at the massive end. The mass function of EMD models features a steeper decline at the massive end, and therefore, at a fixed mass, the same level of a horizontal shift of mass function will give rise to a larger decrease in minihalo abundance.

From the comparisons shown in this section, we can conclude that the model variations have little impact even quantitatively on the mass function and survival fraction of minihaloes up to the mass shift noted previously. The estimated mass survival fraction of minihaloes in the Solar neighborhood is about 60%.

5.4 Galactic survival fraction

In Figure 13, we show the survival (mass) fraction of minihaloes after stellar and tidal disruption as a function of the radius of observation. We choose the fiducial AMC and EMD models (with $m_a = 25 \mu\text{eV}$ and $T_{\text{rh}} = 30 \text{ MeV}$) for comparison here. The number of surviving minihaloes is evaluated by integrating the mass function in three mass bins: $\log (M/M_{\odot}) \in [-12, -10], (-10, -8], (-8, +\infty)$. For both models, the survival fraction of minihaloes significantly drops with increasing minihalo mass and decreasing galactocentric

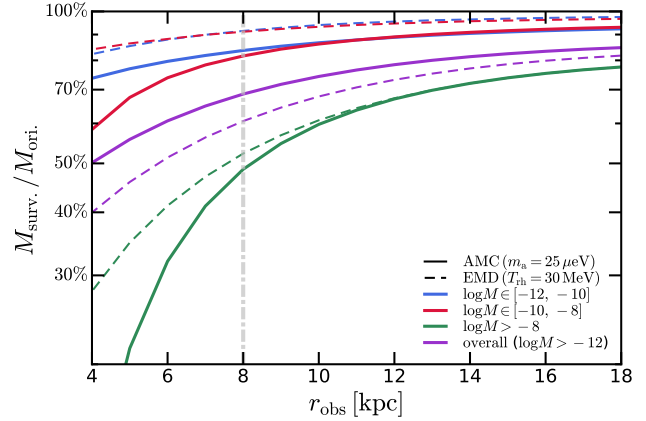


Figure 13. Mass survival fraction of minihaloes as a function of galactocentric distance. In addition to the overall survival fraction after stellar and tidal disruptions, we also show the survival (mass) fraction of minihaloes in three mass bins: $\log (M_{\text{mh}}/[M_{\odot}]) \in [-12, -10], (-10, -8], (-8, \infty)$. Massive minihaloes are more severely disrupted with $\lesssim 50\%$ of the minihalo in the $(-8, \infty)$ bin survived at the Solar neighborhood. On the other hand, low-mass minihaloes in the $[-12, -10]$ bin have $\gtrsim 70\%$ survival fraction at any radius.

distance. Quantitatively, more than 70% of minihaloes in the mass range $\log (M/M_{\odot}) \in [-12, -10]$ survive at any radius of observation, as opposed to $\lesssim 40\%$ survival fraction of minihaloes with $\log (M/M_{\odot}) > -8$ at $r_{\text{obs}} \lesssim 6 \text{ kpc}$. Low-mass minihaloes are less vulnerable to disruption with more concentrated structures, although the survival fraction still decreases sharply at small galactocentric radii due to enhanced stellar surface density. We do not extend this to $r < 4 \text{ kpc}$. The bulge component will take over, lowering the survivability of minihaloes even further.

We expect a high overall survival fraction of $\gtrsim 60\%$ (dominated by the concentrated minihaloes with low masses). But the survival fraction of the most massive QCD axion miniclusters or EMD minihaloes in the Solar neighborhood can drop significantly because of their diluted structures from the hierarchical assembly. In summary, our findings are encouraging for the prospects of axion direct detection in the post-inflationary scenario, because

- Most of the surviving minihaloes are cores with very high densities. We have shown in Figure 6 in Section 3 that the stellar disruption has a limited impact on the central core but primarily destroys the outer shells of the minihalo. The density profile at the outskirts of the minihalo remains steeper than the NFW profile even after the minihalo has fully relaxed from the previous encounter. Local measurements like PTAs may be sensitive to axion minihaloes after disruption since they can potentially probe a mass fraction ($df/d\log M$) well below $\sim 10\%$ (e.g., Dror et al. 2019; Ramani et al. 2020; Lee et al. 2021a).

- As a result of the disruption events, we expect a non-negligible fraction of free axions in the Solar neighborhood. These free axions could impact direct detection signals in axion haloscope experiments (e.g., Asztalos et al. 2010; Graham et al. 2015; Du et al. 2018).

We leave the calculations of astrophysical signals of dark matter minihaloes in the Milky Way for a follow-up study.

6 CONCLUSIONS

In this paper, we systematically studied the environmental effects on dark matter minihaloes (as light as $10^{-12} M_{\odot}$) after infall to the Milky Way. Due to the extensive dynamic range, it is impossible to simultaneously track the evolution of minihaloes in a standard cosmological simulation of the Milky Way-mass galaxy. Therefore, we developed a framework to combine small-scale, idealized N-body simulations with an analytic model of the Milky Way galaxy to make these sorts of predictions tractable.

Stellar disruption and tidal disruption are the most critical environmental effects. For stellar disruption, the analytic expressions in the literature are inadequate to accurately capture the minihalo mass loss after stellar encounters. To address this, we developed a semi-analytic model calibrated by a suite of N-body simulations of idealized encounters between a star and a minihalo, varying impact parameters, minihalo masses, and concentrations. On the other hand, for tidal disruption, our N-body simulations show that the disruption effects can be predicted accurately by relatively simple analytic models. To connect to galactic scales, we apply a simplified orbital model of minihaloes and derive an orbital-averaged treatment of stellar and tidal disruptions. We perform Monte Carlo simulations to model the mass evolution of minihaloes with various masses, concentrations, and infall histories. The framework allows us to make predictions for survival fraction of minihaloes in the Milky Way as a function of galactocentric radius and halo parameters. This paper focuses on the miniclusters of post-inflationary axions and minihaloes in the Early Matter Domination. However, the same framework can be easily applied to other types of dark matter substructure models. Our major findings can be summarized below:

- When the energy imparted (ΔE) during a stellar encounter is much smaller than the binding energy of the minihalo (E_b), the mass loss is relatively insensitive to minihalo concentration. However, when $\Delta E/E_b$ exceeds unity and continues to increase, minihaloes with lower concentration will experience significantly larger mass loss in stellar encounters. This aspect has not been considered in previous studies of dark matter substructures.

- For tidal disruption, we confirm the existence of a tidal radius outside which minihaloes are largely stripped. The analytical formula works remarkably well even for extremely light minihaloes ($M_{\text{mh}} \sim 10^{-8} M_{\odot}$). On the other hand, the stellar disruption results in a shell of marginally-bound particles propagating outwards, leaving a characteristic density profile similar to the Hernquist profile at large radii. The stellar disruption can also slightly reduce the minihalo central densities.

- We show that there could be non-trivial non-linear interactions/combined effects between these disruption processes. The first tidal or stellar disruption will leave dense cores of the original minihaloes, which are typically less vulnerable to future disruptions. Therefore, the assumptions on the structures of minihaloes need to be revised. Our analytic method includes analytical corrections on minihalo structural parameters after tidal disruptions. For stellar disruptions, we use the accumulated injected energy to compute the stellar disruption fraction, which effectively accounts for successive stellar encounters progressively stripping the outskirts of minihaloes.

- Applying our methods to well-motivated models like post-inflationary AMC and EMD minihaloes, we find a relatively stable mass survival fraction of $\sim 60\%$ at the Solar neighborhood. The number is insensitive to model choices. Over the entire mass range of interest, stellar encounter is the dominant disruption mechanism. The remaining minihaloes are abundant and dense enough to give direct detection signals in *e.g.* upcoming PTA observations.

The follow-up paper will focus on direct detection signals of minihaloes. In the future, the framework built in this paper can be applied to a spectrum of interesting topics in particle astrophysics, such as the dark matter annihilation rate in minihaloes and axion minicluster-neutron star encounters.

ACKNOWLEDGEMENTS

We thank Andrea Mitridate for useful discussions on the mass-concentration relation and Gabriel Aguiar for the collaboration in the early stages of this work. HX is supported in part by the United States Department of Energy (DOE) under grant number DE-SC0011637. KZ is supported by a Simons Investigator award and the U.S. DOE, Office of Science, Office of High Energy Physics, under Award No. DE-SC0011632. Support for XS and PFH was provided by the National Science Foundation (NSF) Research Grants 1911233, 20009234, 2108318, NSF CAREER grant 1455342, the National Aeronautics and Space Administration (NASA) grants 80NSSC18K0562, HST-AR-15800. Numerical calculations were run on the Caltech computing cluster “Wheeler”, allocations AST21010 and AST20016 supported by the NSF and the Texas Advanced Computing Center (TACC), and NASA HEC SMD-16-7592.

DATA AVAILABILITY

The simulation data of this work was generated and stored on the computing system “Wheeler” at California Institute of Technology. The code for the semi-analytic model and the summary of simulation results are available at [the project repository](#). The raw data of the idealized simulations will be shared on reasonable request to the corresponding author.

REFERENCES

- Aghanim N., et al., 2020, *Astron. Astrophys.*, 641, A6
 Angus G. W., Zhao H., 2007, *MNRAS*, 375, 1146
 Asztalos S. J., et al., 2010, *Phys. Rev. Lett.*, 104, 041301
 Baghran S., Afshordi N., Zurek K. M., 2011, *Phys. Rev. D*, 84, 043511
 Barnes J. E., Hernquist L., 1992, *ARA&A*, 30, 705
 Berezhinsky V., Dokuchaev V., Eroshenko Y., 2003, *Phys. Rev. D*, 68, 103003
 Berezhinsky V. S., Dokuchaev V. I., Eroshenko Y. N., 2014, *Physics Uspekhi*, 57, 1
 Binney J., Tremaine S., 1987, Galactic dynamics
 Bland-Hawthorn J., Gerhard O., 2016, *ARA&A*, 54, 529
 Blinov N., Dolan M. J., Draper P., 2020, *Phys. Rev. D*, 101, 035002
 Blinov N., Dolan M. J., Draper P., Shelton J., 2021, *Phys. Rev. D*, 103, 103514
 Boylan-Kolchin M., Ma C.-P., Quataert E., 2005, *MNRAS*, 362, 184
 Bullock J. S., Boylan-Kolchin M., 2017, *ARA&A*, 55, 343
 Bullock J. S., Kolatt T. S., Sigad Y., Somerville R. S., Kravtsov A. V., Klypin A. A., Primack J. R., Dekel A., 2001, *MNRAS*, 321, 559
 Buschmann M., Foster J. W., Safdi B. R., 2020, *Phys. Rev. Lett.*, 124, 161103
 Buschmann M., Foster J. W., Hook A., Peterson A., Willcox D. E., Zhang W., Safdi B. R., 2022, *Nature Commun.*, 13, 1049
 Carr B. J., Sakellariadou M., 1999, *ApJ*, 516, 195
 Chen J., Du X., Lentz E. W., Marsh D. J. E., Niemeyer J. C., 2021, *Phys. Rev. D*, 104, 083022
 D’Onghia E., Springel V., Hernquist L., Keres D., 2010, *ApJ*, 709, 1138
 Dai L., Miralda-Escudé J., 2020, *The Astronomical Journal*, 159, 49
 Deason A. J., Belokurov V., Evans N. W., An J., 2012, *MNRAS*, 424, L44
 Dehnen W., 1993, *MNRAS*, 265, 250
 Delos M. S., 2019, *Phys. Rev. D*, 100, 083529
 Diaz Rivero A., Cyr-Racine F.-Y., Dvorkin C., 2018, *Phys. Rev. D*, 97, 023001

- Diemer B., Kravtsov A. V., 2014, *ApJ*, **789**, 1
- Dror J. A., Ramani H., Trickle T., Zurek K. M., 2019, *Phys. Rev. D*, **100**, 023003
- Du N., et al., 2018, *Phys. Rev. Lett.*, **120**, 151301
- Eggeheimer B., Redondo J., Dolag K., Niemeyer J. C., Vaquero A., 2020, *Phys. Rev. Lett.*, **125**, 041301
- Enander J., Pargner A., Schwetz T., 2017, *JCAP*, **12**, 038
- Erickcek A. L., Sigurdson K., 2011, *Phys. Rev. D*, **84**, 083503
- Facchinetti G., Stref M., Lavalle J., 2022, arXiv e-prints, p. arXiv:2201.09788
- Fairbairn M., Marsh D. J. E., Quevillon J., Rozier S., 2018, *Phys. Rev. D*, **97**, 083502
- Fan J., Özsoy O., Watson S., 2014, *Phys. Rev. D*, **90**, 043536
- Feldmann R., et al., 2022, arXiv e-prints, p. arXiv:2205.15325
- Gerhard O. E., Fall S. M., 1983, *MNRAS*, **203**, 1253
- Gnedin O. Y., Hernquist L., Ostriker J. P., 1999, *ApJ*, **514**, 109
- Goerdt T., Gnedin O. Y., Moore B., Diemand J., Stadel J., 2007, *MNRAS*, **375**, 191
- Gorghetto M., Hardy E., Villadoro G., 2021, *SciPost Phys.*, **10**, 050
- Graham P. W., Irastorza I. G., Lamoreaux S. K., Lindner A., van Bibber K. A., 2015, *Annual Review of Nuclear and Particle Science*, **65**, 485
- Graham P. W., Mardon J., Rajendran S., 2016, *Phys. Rev. D*, **93**, 103520
- Green A. M., Goodwin S. P., 2007, *Monthly Notices of the Royal Astronomical Society*, **375**, 1111–1120
- Green A. M., Hofmann S., Schwarz D. J., 2005, *J. Cosmology Astropart. Phys.*, **2005**, 003
- Green S. B., van den Bosch F. C., Jiang F., 2021, *MNRAS*, **503**, 4075
- Grudić M. Y., Hopkins P. F., 2020, *Monthly Notices of the Royal Astronomical Society*, **495**, 4306
- Helfer T., Marsh D. J. E., Clough K., Fairbairn M., Lim E. A., Becerril R., 2017, *JCAP*, **03**, 055
- Hernquist L., 1990, *ApJ*, **356**, 359
- Hernquist L., Quinn P. J., 1987, *ApJ*, **312**, 1
- Hernquist L., Quinn P. J., 1988, *ApJ*, **331**, 682
- Hernquist L., Spergel D. N., 1992, *ApJ*, **399**, L117
- Hernquist L., Spergel D. N., Heyl J. S., 1993, *ApJ*, **416**, 415
- Herpich J., Stinson G. S., Rix H. W., Martig M., Dutton A. A., 2017, *MNRAS*, **470**, 4941
- Hofmann S., Schwarz D. J., Stöcker H., 2001, *Phys. Rev. D*, **64**, 083507
- Hogan C. J., Rees M. J., 1988, *Phys. Lett. B*, **205**, 228
- Hopkins P. F., 2015, *MNRAS*, **450**, 53
- Hopkins P. F., Hernquist L., Cox T. J., Younger J. D., Besla G., 2008, *ApJ*, **688**, 757
- Hopkins P. F., Lauer T. R., Cox T. J., Hernquist L., Kormendy J., 2009, *ApJS*, **181**, 486
- Hopkins P. F., Kereš D., Oñorbe J., Faucher-Giguère C.-A., Quataert E., Murray N., Bullock J. S., 2014, *MNRAS*, **445**, 581
- Hopkins P. F., et al., 2018a, *MNRAS*, **480**, 800
- Hopkins P. F., et al., 2018b, *Mon. Not. Roy. Astron. Soc.*, **480**, 800
- Howlett C., Lewis A., Hall A., Challinor A., 2012, *J. Cosmology Astropart. Phys.*, **1204**, 027
- Katz A., Kopp J., Sibiryakov S., Xue W., 2018, *J. Cosmology Astropart. Phys.*, **2018**, 005
- Kavanagh B. J., Edwards T. D. P., Visinelli L., Weniger C., 2020, Stellar Disruption of Axion Miniclusters in the Milky Way (arXiv:2011.05377)
- Kawasaki M., Kohri K., Sugiyama N., 1999, *Phys. Rev. Lett.*, **82**, 4168
- King I., 1962, *AJ*, **67**, 471
- Klypin A., Zhao H., Somerville R. S., 2002, *ApJ*, **573**, 597
- Kolb E. W., Tkachev I. I., 1993, *Phys. Rev. Lett.*, **71**, 3051
- Kolb E. W., Tkachev I. I., 1994, *Phys. Rev. D*, **49**, 5040
- Kolb E. W., Tkachev I. I., 1996, *Astrophys. J. Lett.*, **460**, L25
- Kroupa P., 2001, *MNRAS*, **322**, 231
- Kroupa P., Tout C. A., Gilmore G., 1993, *MNRAS*, **262**, 545
- Lee V. S. H., Mitridate A., Trickle T., Zurek K. M., 2021a, *JHEP*, **06**, 028
- Lee V. S. H., Taylor S. R., Trickle T., Zurek K. M., 2021b, *JCAP*, **08**, 025
- Lewis A., , CAMB Notes, <https://cosmologist.info/notes/CAMB.pdf>
- Lewis A., Challinor A., Lasenby A., 2000, *ApJ*, **538**, 473
- Loeb A., Zaldarriaga M., 2005, *Phys. Rev. D*, **71**, 103520
- McMillan P. J., 2011, *MNRAS*, **414**, 2446
- McMillan P. J., 2017, *MNRAS*, **465**, 76
- Metcalf R. B., Madau P., 2001, *Astrophys. J.*, **563**, 9
- Mo H. J., Mao S., White S. D. M., 1998, *MNRAS*, **295**, 319
- Moore B., 1993, *ApJ*, **413**, L93
- More S., Diemer B., Kravtsov A. V., 2015, *ApJ*, **810**, 36
- Moster B. P., Naab T., White S. D. M., 2013, *MNRAS*, **428**, 3121
- Navarro J. F., Frenk C. S., White S. D. M., 1996, *ApJ*, **462**, 563
- Navarro J. F., Frenk C. S., White S. D. M., 1997, *ApJ*, **490**, 493
- Nelson A. E., Scholtz J., 2011, *Phys. Rev. D*, **84**, 103501
- Oguri M., Lee J., 2004, *MNRAS*, **355**, 120
- Ostriker J. P., Spitzer Lyman J., Chevalier R. A., 1972, *ApJ*, **176**, L51
- Peccei R. D., Quinn H. R., 1977, *Phys. Rev. Lett.*, **38**, 1440
- Power C., Navarro J. F., Jenkins A., Frenk C. S., White S. D. M., Springel V., Stadel J., Quinn T., 2003, *MNRAS*, **338**, 14
- Press W. H., Schechter P., 1974, *ApJ*, **187**, 425
- Pullen A. R., Benson A. J., Moustakas L. A., 2014, *ApJ*, **792**, 24
- Ramani H., Trickle T., Zurek K. M., 2020, *JCAP*, **12**, 033
- Scalo J. M., 1986, *Fundamentals of Cosmic Physics*, **11**, 1
- Schneider A., Krauss L., Moore B., 2010, *Phys. Rev. D*, **82**, 063525
- Siegel E. R., Hertzberg M. P., Fry J. N., 2007, *Mon. Not. Roy. Astron. Soc.*, **382**, 879
- Sollima A., 2019, *MNRAS*, **489**, 2377
- Somerville R. S., et al., 2018, *MNRAS*, **473**, 2714
- Spitzer Lyman J., 1958, *ApJ*, **127**, 17
- Springel V., 2005, *MNRAS*, **364**, 1105
- Stref M., Lavalle J., 2017, *Phys. Rev. D*, **95**, 063003
- Taffoni G., Mayer L., Colpi M., Governato F., 2003, *MNRAS*, **341**, 434
- Taylor J. E., Babul A., 2001, *ApJ*, **559**, 716
- Tremaine S., Richstone D. O., Byun Y.-I., Dressler A., Faber S. M., Grillmair C., Kormendy J., Lauer T. R., 1994, *AJ*, **107**, 634
- Van Tilburg K., Taki A.-M., Weiner N., 2018, *JCAP*, **07**, 041
- Visinelli L., Baum S., Redondo J., Freese K., Wilczek F., 2018, *Phys. Lett. B*, **777**, 64
- Wechsler R. H., Bullock J. S., Primack J. R., Kravtsov A. V., Dekel A., 2002, *ApJ*, **568**, 52
- Xiao H., Williams I., McQuinn M., 2021, *Phys. Rev. D*, **104**, 023515
- Zentner A. R., Bullock J. S., 2003a, *ApJ*, **598**, 49
- Zentner A. R., Bullock J. S., 2003b, *ApJ*, **598**, 49
- Zentner A. R., Berlind A. A., Bullock J. S., Kravtsov A. V., Wechsler R. H., 2005, *ApJ*, **624**, 505
- Zhao H., Hooper D., Angus G. W., Taylor J. E., Silk J., 2007, *ApJ*, **654**, 697
- Zurek K. M., Hogan C. J., Quinn T. R., 2007, *Phys. Rev. D*, **75**, 043511
- van den Bosch F. C., Lewis G. F., Lake G., Stadel J., 1999, *ApJ*, **515**, 50
- van den Bosch F. C., Ogiya G., Hahn O., Burkert A., 2018, *MNRAS*, **474**, 3043

APPENDIX A: THE MINIHALO MASS FUNCTION AND CONCENTRATION IN DIFFERENT MODELS

The minihalo mass function arising from an enhanced matter power spectrum at small scales can be considered separately from the adiabatic power spectrum. We use the Press-Schechter model to compute the minihalo mass function (Press & Schechter 1974)

$$\frac{M^2 dn/dM}{\bar{\rho}} \frac{dM}{M} = \nu f(\nu) \frac{d\nu}{\nu}, \quad (\text{A1})$$

where $\bar{\rho}$ is the comoving density of dark matter and ν is a dimensionless parameter that defines the rareness of the halo. $f(\nu)$ and ν are defined as

$$\nu f(\nu) = \sqrt{\frac{\nu}{2\pi}} \exp(-\nu/2), \quad (\text{A2})$$

$$\nu \equiv \frac{\delta_c^2(z)}{\sigma^2(M)},$$

where $\delta_c = 1.686$ is the critical density required for the formation of collapsed haloes in spherical collapse models. $\sigma^2(M)$ is the variance of the initial perturbations smoothed with a top-hat filter of scale $R = (3M/4\pi\bar{\rho})^{1/3}$, which can be determined as

$$\sigma^2(M) \equiv \int \frac{dk}{k} \frac{k^3 P(k)}{2\pi^2} D_1^2(z) |W(kR)|^2, \quad (\text{A3})$$

where $W(x) = (3/x^3)[\sin(x) - x\cos(x)]$ is the spherical top-hat window function, $D_1(z)$ is the growth function normalized in the radiation era, and $P(k)$ is the primordial matter power spectrum introduced by new physics, such as axions. The variance of white-noise power spectrum from the axion in the post-inflationary scenario can be expressed as

$$\sigma(M) = D_1(z) \sqrt{\frac{3A_{\text{osc}} M_0}{2\pi^2 M}}, \quad (\text{A4})$$

where A_{osc} is the amplitude of the white-noise power spectrum, which is taken to be 0.1 in this work. M_0 can be determined from the QCD axion mass (Dai & Miralda-Escudé 2020; Xiao et al. 2021)

$$M_0 = 2.3 \times 10^{-10} \left(\frac{50 \mu\text{eV}}{m_a} \right)^{0.51} M_\odot. \quad (\text{A5})$$

Given the value of M_0 , one can obtain the minihalo mass function using the Press-Schechter model if the adiabatic fluctuations are neglected. It is worth noting that the variance is a function of M/M_0 , such that the shape of the mass function will remain the same when we change the model parameters but the characteristic mass will shift accordingly.

In the early matter domination scenario, the minihalo mass function can be calculated with a similar method. In this scenario, the primordial power spectrum remain the same as the adiabatic fluctuations but their growth is modified. Effectively, this is enhancing the primordial power spectrum at small scales. The reheating temperature T_{rh} is the only relevant physical parameter that determines the characteristic scale of the matter power spectrum, which corresponds to a characteristic mass scale M_{rh} . The variance is enhanced at small scales due to early matter domination, in a manner which scales as

$$\sigma(M \lesssim M_{\text{rh}}) \propto D_1(z) (M/M_{\text{rh}})^{-(n+3)/6}, \quad (\text{A6})$$

where $n = 0.963$ is the scalar spectral index (Erickcek & Sigurdson 2011) and $M_{\text{rh}} \approx 9.06 \times 10^{-5} M_\odot (10\text{MeV}/T_{\text{rh}})^3$. Similar to the axion minicluster scenario, the variance is only a function of M/M_{rh} and the shape does not change with the reheating temperature. Thus we can compute the minihalo mass function based on the variance using Press-Schechter. We can further compute the mass function including minihaloes that have fallen into the massive CDM haloes by including the effect of adiabatic fluctuations, as shown in Figure 12.

APPENDIX B: CONVERGENCE TESTING ON THE SIMULATION OF STELLAR DISRUPTIONS

Briefly here we discuss numerical tests of the simulations of stellar disruptions. The fiducial simulations presented in the main text employ the constant gravitation softening length 10^{-9} kpc and dark matter particle mass resolution $10^{-16} M_\odot$ for minihaloes with a mass of $10^{-10} M_\odot$. We cap the timestep at 10^{-8} Gyr during the stellar encounter to resolve the star trajectory since the stellar disruption is mostly relevant during the crossing. We justify those choices in more detail here.

B1 Gravitational softening

The gravitational softening length must be chosen appropriately in the simulation so that we can resolve the relevant physical scales. In our idealized simulations of stellar disruption, the minimum halo mass is $10^{-10} M_\odot$ which corresponds to a scale radius of $r_s = 9.6 \times 10^{-8}$ kpc at $z = 0$. With the fiducial particle mass resolution, the convergence radius of dark matter calculated using the Power et al. (2003) criterion is $\sim 10^{-8}$ kpc. Therefore, the fiducial gravitational softening length, 10^{-9} kpc, and particle mass resolution should be sufficient to resolve the core profile of the halo. An additional run was performed with a gravitational softening length 2×10^{-9} kpc and the results of the disruption fraction and mass profile are robust. We have also verified that the results are robust to particle number at our fiducial resolution.

B2 Time-stepping

Since the crossing time of a stellar encounter is orders-of-magnitude shorter than the internal dynamical time of the minihalo, we need sufficiently small timesteps to resolve the trajectory of the star at the vicinity of the minihalo. The time-stepping parameter in our fiducial simulations is capped at 10^{-8} Gyr, which is roughly $1/5 R_{\text{mh}}/v_*$, where R_{mh} is the minihalo radius and the corresponding minihalo mass is $10^{-10} M_\odot$. In an additional run, the time-stepping parameter is changed to 2×10^{-8} Gyr while other parameters including the minihalo parameters are exactly the same. We obtain the same disruption fraction, mass profile, and energy change after the halo is fully relaxed.

APPENDIX C: ORBITAL MODEL OF MINIHALOES

The analytic calculation of accumulated energy in Equation 28 comes from only one encounter with the minihalo velocities perpendicular to the plane of the Galactic disk. In reality, minihaloes after infall to the Milky Way halo will typically cross the stellar disks multiple times at various locations. To measure the accumulated energy input from a series of disk crossings, we need to evaluate the total number of passages through the disk, the stellar surface density where the encounter occurs and the angle of incidence, with an ensemble average over all possible orbits for the minihaloes eventually found at the observed radius.

For simplicity, we adopt a singular isothermal sphere model following the method in van den Bosch et al. (1999) to estimate the uncertainties related to the orbits of minihaloes. The density and potential of the system are given by

$$\rho = \frac{V_c^2}{4\pi G r^2}, \quad \Phi = V_c^2 \ln(r/r_0), \quad (\text{C1})$$

where V_c is the constant circular velocity assumed to be 200 km/s and r_0 is the point of zero potential assumed to be 10 kpc. For a bound test particle in this potential, its halocentric distance r will oscillate between the peri and apocenter with the period

$$T = 2 \int_{r_1}^{r_2} \frac{dr}{\sqrt{2[E - \Phi(r)] - L^2/r^2}}, \quad (\text{C2})$$

where r_1 and r_2 are the peri and apocenter of the orbit, which can be determined by solving the equation

$$\frac{1}{r^2} + \frac{2[\Phi(r) - E]}{L^2} = 0. \quad (\text{C3})$$

Due to the scale-free nature of the singular isothermal profile, the

equations can be simplified by defining the maximum angular momentum $L_c(E) = r_c(E)V_c$, where $r_c(E)$ is the radius of the circular orbit with energy E given by

$$r_c(E) = r_0 \exp\left(\frac{E}{V_c^2} - \frac{1}{2}\right) \quad (\text{C4})$$

Based on this, the circularity parameter is defined as $\eta = L/L_c(E)$ and Equation C3 is reduced to

$$\frac{1}{x^2} + \frac{2 \ln(x)}{\eta^2} - \frac{1}{\eta^2} = 0, \quad (\text{C5})$$

where $x \equiv r/r_c$ and the two solutions correspond to the peri and apocenter distances, which are independent of the energy of the test particle if normalized by $r_c(E)$. Similarly, if normalized by $r_c(E)/V_c$, T also becomes independent of E . The look-up tables of T , r_1 and r_2 with respect to η are computed numerically. Here we do not consider the scattering and mergers of minihaloes within the parent halo and treat their orbits as unperturbed from various relaxation mechanisms.

Assuming spherical symmetry, the ergodic phase-space distribution function $f(\epsilon)$ can be derived through the Eddington inversion method

$$f(\epsilon) = \frac{1}{\sqrt{8}\pi^2} \frac{d}{d\epsilon} \int_0^\epsilon \frac{d\psi}{\sqrt{\epsilon - \psi}} \frac{d\rho}{d\psi}, \quad (\text{C6})$$

where $\psi \equiv -\Phi$ and $\epsilon \equiv -E$. For the singular isothermal profile, the solution is simply the Boltzmann distribution

$$g(E) = K \exp(-2E/V_c^2), \quad (\text{C7})$$

where K is a constant normalization factor. Given a target radius for observation r_{obs} , the normalized phase-space probability density function (PDF) of dark matter particles localized around r_{obs} is

$$f(E, L)|_{r_{\text{obs}}} = \frac{4\pi}{r_{\text{obs}}^2 \rho(r_{\text{obs}})} \frac{g(E) L}{\sqrt{2(E - \Phi(r_{\text{obs}})) - L^2/r_{\text{obs}}}}, \quad (\text{C8})$$

where $E \geq \Phi(r_{\text{obs}})$ and $L \leq 2r_{\text{obs}}\sqrt{E - \Phi(r_{\text{obs}})}$ are required. Replacing L as $\eta L_c(E)$, we obtain

$$f(E, \eta)|_{r_{\text{obs}}} = \frac{4\pi}{r_{\text{obs}} \rho(r_{\text{obs}})} g(E) L_c(E) \frac{\eta}{\sqrt{\eta_{\text{max}}^2 - \eta^2}}, \quad (\text{C9})$$

where $\eta \leq \eta_{\text{max}} = r_{\text{obs}}\sqrt{2(E - \Phi(r_{\text{obs}}))}/L_c(E)$. Following van den Bosch et al. (1999), we perform a Monte Carlo sampling of particles in the phase space based on this distribution function. For each sample particle, we compute its orbital period T , pericenter and apocenter distances r_1 and r_2 based on the look-up table created earlier. We note that because of the self-similar nature of the isothermal sphere, the value of r_1 and r_2 with respect to r_{obs} is independent of r_{obs} , similarly for $T/T_{\text{circ}}(r_{\text{obs}})$. In Figure C1, we show the probability distribution function (PDF) of eccentricities, pericenter and apocenter distances and orbital periods of sampled minihalo orbits. The distribution should be self-similar for any target radius of observation. In the left panel of Figure C1, we compare the distribution of eccentricity derived here with that from van den Bosch et al. (1999) which match perfectly. In the right panel of Figure C1, we compute the mean value of $N_p/N_p^{\text{circ}} = T_{\text{circ}}/T$ which gives us the correction factor for the number of passages through the stellar disk (compared to the circular orbit case) as $f_{N_p} \equiv \langle N_p \rangle_o / N_p^{\text{circ}} \approx 1.3$. $\langle \rangle_o$ denotes averaging over all possible minihalo orbits. This correction factor is independent of the target radius of observation.

Assuming spherical symmetry, the orbit of a test particle will be confined in a plane and the precession of the orbit will eventually lead to a rosette-like pattern. The phase of the precession when the

orbit crosses the disk plane is random. Considering a large ensemble of dark matter particles, the distribution of the radial location where the encounter with the stellar disk takes place will be the same as the probability of the presence of the particle at that distance, and thus equivalent to the time-averaged radial distance of the test particle. Therefore, we have the averaged surface density given the orbit parameter E, L as

$$\langle \Sigma_* \rangle_x(E, L) = \frac{2}{T} \int_{r_1}^{r_2} \frac{\Sigma_*(r) dr}{\sqrt{2[E - \Phi(r)] - L^2/r^2}}, \quad (\text{C10})$$

where $\langle \rangle_x$ denotes averaging over all past disk crossings and the stellar surface density profile $\Sigma_*(r)$ is given below Equation 23 following the measurements in McMillan (2011, 2017). The average of the second order term $\langle \Sigma_*^2 \rangle_x$ can be obtained in a similar fashion. In the top panel of Figure C2, we show the distribution of $\langle \Sigma_* \rangle_x / \Sigma_*(r_{\text{obs}})$ at the target radius 8 kpc and the correction factor $f_{\Sigma_*}(r_{\text{obs}}) \equiv \langle \langle \Sigma_* \rangle_x / \Sigma_*(r_{\text{obs}}) \rangle_o$ (averaging over all possible orbits) is about 1.16. We compute the value of f_{Σ_*} and $f_{\Sigma_*^2}$ at several different r_{obs} from 2 to 16 kpc and find that both $f_{\Sigma_*}(r_{\text{obs}})$ and $f_{\Sigma_*^2}(r_{\text{obs}})$ can be fitted by the functional form $A e^{B+(r_{\text{obs}}/r_c)^\alpha}$. The best-fit parameters are $A = 0.106, B = 2.03, r_c = 12.961, \alpha = 2.048$ for f_{Σ_*} and $A = 0.318, B = 0.781, r_c = 5.740, \alpha = 1.628$ for $f_{\Sigma_*^2}$.

An additional correction comes from the enhanced surface density when the minihalo trajectory is not perpendicular to the disk plane. To leading order, the effective surface density along the trajectory of the incident minihalo (as well as the time duration the minihalo stays in the disk) should scale as $1/\cos\theta$. Assuming the velocities of dark matter particles are isotropic, the correction factor is

$$f_\theta = \left\langle \frac{1}{\cos\theta} \right\rangle = \int_{H/r_d}^1 \frac{d\cos\theta}{\cos\theta} = \ln(r_d/H_d) \approx 2, \quad (\text{C11})$$

where we have imposed a cut-off at $\cos\theta = H_d/r_d$ with H_d and r_d the scale height and length of the disk, assuming to be 400 pc and 3 kpc, respectively. Particles with even smaller incidence angles stay in the disk and will become completely disrupted (see Equation 23) which will have no impact on the averaged energy imparted. Combine the two effects above, we obtain the correction factor for the effective stellar surface density.

This paper has been typeset from a $\text{\TeX}/\text{\LaTeX}$ file prepared by the author.

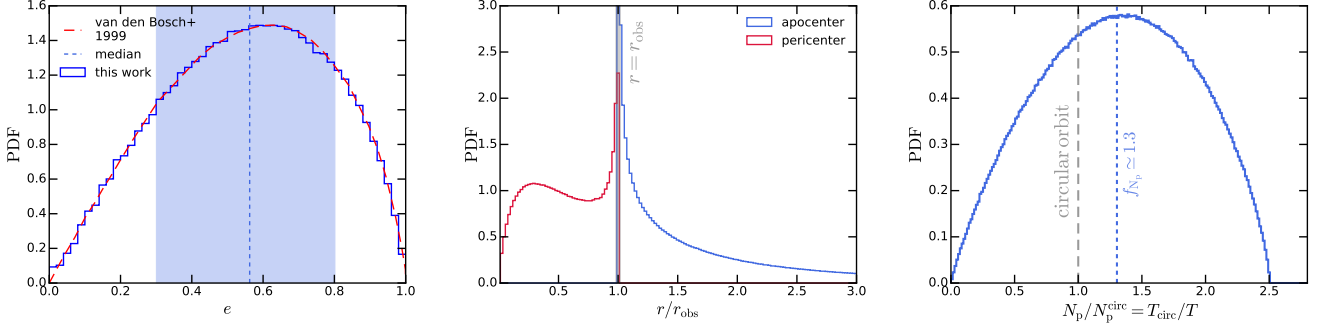


Figure C1. Distribution of eccentricities (left), pericenter and apocenter distances (middle) and orbital periods (or equivalently N_p , right).

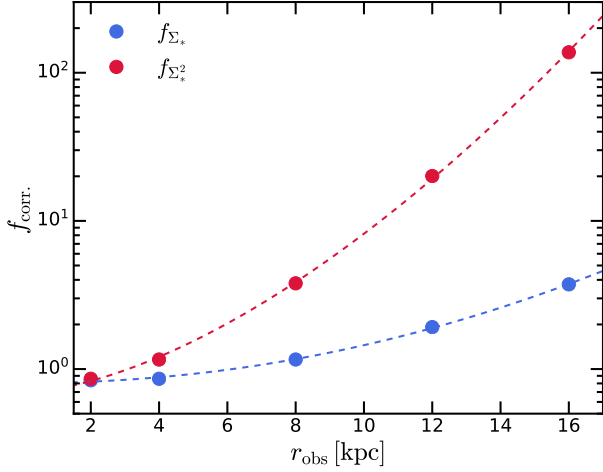
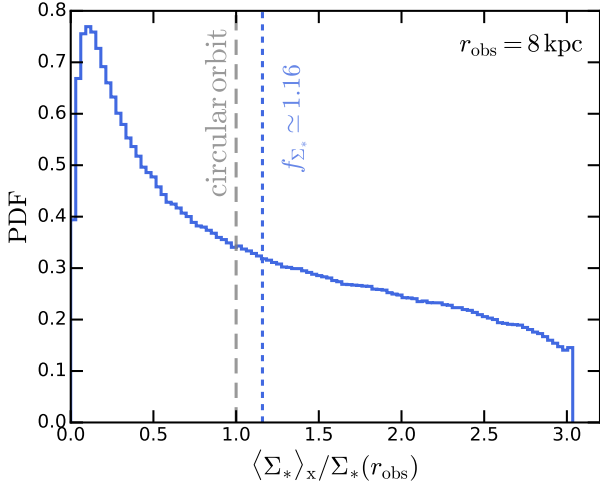


Figure C2. *Top:* Distribution of the surface density averaged over all past disk crossings. *Bottom:* The correction factor for Σ_* and Σ_*^2 as a function of r_{obs} .